THE ASTROPHYSICAL JOURNAL, 418:82–99, 1993 November 20

MODELING THE SPATIAL DISTRIBUTION OF STAR FORMATION IN INTERACTING DISK GALAXIES

J. CHRISTOPHER MIHOS[1,2]
Department of Astronomy, University of Michigan, Ann Arbor, MI 48109
GREGORY D. BOTHUN[1]
Department of Physics, University of Oregon, Eugene, OR 97403
AND
DOUGLAS O. RICHSTONE
Department of Astronomy, University of Michigan, Ann Arbor, MI 48109
Received 1993 January 19; accepted 1993 May 26

ABSTRACT

Models of star-forming interacting galaxies are combined with observational data to investigate the nature of star formation in interacting and merging disk galaxies. Detailed models of specific interacting systems are created using the observed morphology and kinematics of the system to constrain model parameters describing the interaction. The models employ an N-body code to calculate the gravitational dynamics, a discrete cloud model to govern the ISM dynamics, and a modified Schmidt law to describe star formation. To compare the models to the observed systems, new observations of three interacting systems—NGC 4676, IC 1908, and NGC 6872/IC 4970—are presented, along with observations of NGC 4038/39 and NGC 7252 culled from the literature. The resulting modeled star-forming properties of each system are then compared to observed star formation tracers such as the spatial distribution of Hα and the total far-infrared luminosity.

We find that the models describe the star-forming properties of several observed systems reasonably well in terms of the relative intensity and morphology of induced star formation. In several cases, however, the models underestimate the star formation rate in regions where the ISM is presumed to be experiencing a strong collision, suggesting that collisionally induced star formation may play an important role in such regions. Furthermore, strong star formation is observed in regions of high-velocity dispersion and velocity gradients in Fabry-Perot observations of both IC 1908 and NGC 6872. Finally, the relatively mild modeled starbursts in the merging systems again show the difficulty in triggering starbursts intense enough to drive the emission from ultraluminous infrared galaxies. In order to trigger such activity via merger-induced star formation, the merger must occur rapidly and involve extremely gas rich disks.

Subject headings: galaxies: interactions — galaxies: stellar content — stars: formation

1. INTRODUCTION

The degree to which interactions between galaxies elevate their respective star formation rates must depend upon both the orbital interaction parameters and the density and phase of the gas in the respective interstellar media. However, observations which connect elevated levels of radio, optical, Hα or far-infrared (FIR) emission to interaction morphology (e.g., Larson & Tinsley 1979; Joseph et al. 1984; Bushouse 1987; Kennicutt et al. 1987; Lonsdale, Persson, & Matthews 1984; Hummel 1981; Heckman 1980; Mazzarella, Bothun, & Boroson 1991) fail to reveal which alternative is the dominant one. Moreover, the very large spread in the observed SFRs of morphologically selected samples of interacting galaxies obviously suggests that interactions alone are not sufficient to trigger starburst activity. Hence, the *detailed* nature of star formation in interacting and merging systems remains poorly understood.

To probe the more detailed response of star formation to galaxy encounters, we combine numerical models with high quality observational data, including our own Fabry-Perot observations, of specific interacting systems in order to directly compare the spatial and velocity distribution of star-forming gas with various model parameters. Previous modeling of star formation in interacting systems has focused on general star-forming properties of a range of interaction types (e.g., Noguchi & Ishibashi 1986; Olson & Kwan 1990a, b; Noguchi 1991; Mihos, Richstone, & Bothun 1991, 1992). While such modeling has been used to successfully explain many properties of large samples of interacting systems, important details remain uninvestigated. Our approach here is to create models of several specific interacting systems which span a range of interaction types.

Through a combined examination of the observed properties of each system and the dynamical properties of the system model, the physical conditions of the star-forming environments in each system can be probed. Properties such as the density, velocity dispersion, and kinematics of the ISM can play major roles in driving star-forming events. By examining such properties in specific systems, information on the physical trigger for interaction-induced starbursts can be obtained; a subsequent comparison of the properties exhibited by a range of interactions may shed light on the universality of any such trigger.

[1] Visiting Astronomer, Cerro Tololo Inter-American Observatory. CTIO is operated by AURA, Inc. under contract to the National Science Foundation.
[2] Present address: Board of Studies in Astronomy and Astrophysics, University of California, Santa Cruz, Santa Cruz, CA 95064. E-mail:hos@lick.ucsc.edu.

2. MODELING TECHNIQUE

2.1. *Numerical Models*

The numerical models used in this work have been presented in detail in Mihos et al. (1992, hereafter MRB), and will be described only briefly here. The fully consistent N-body code is based on L. Hernquist's TREECODE (Hernquist 1987), with modifications made to model star formation and interactions between ISM gas clouds. Two types of particles are used: "stellar" particles which act as collisionless mass points and "gaseous" particles which represent gas clouds. The gaseous particles can collide and merge with one another, thereby taking into account the dissipative nature of the ISM. Massive clouds may also fragment into smaller clouds, giving the cloud system a dynamic nature. The mean free path for the clouds is typically ~ 2 kpc, and typical fragmentation times are ~ 20–30 Myr. The star formation rate in a cloud is based on a modified Schmidt law and given by

$$\dot{M}_i = CM_i\rho_i ,$$

where C is a normalization constant, M_i is the cloud mass, and ρ_i is the environmental gas density surrounding the ISM cloud. The normalization constant is chosen such that an isolated galaxy forms stars at a rate of $\sim 1\ M_\odot\ \mathrm{yr}^{-1}$. Averaged over volume, this model closely reproduces a classical Schmidt law of index $n \sim 1.8$. At each time step, the amount of gas formed into stars in each cloud is removed from the cloud mass, thereby realizing the depleting effects of star formation.

Each galaxy consists of three components—a spherical halo, an exponential disk, and a flat distribution of gas clouds representing the ISM. The mass ratio of these components is 4:1:0.2, respectively. The halo and disk consist of 4000 stellar particles each, while the ISM is made of 6000 gaseous particles, yielding a total number of 28,000 particles at the beginning of each simulation. The system of units employed defines $G \equiv 1$, with each galaxy having a total mass of 1.30. The half-mass radius of the halo is 0.56, the disk scale length is 0.25, and the ISM clouds are distributed evenly out to a radius of 1. Scaling these values to physical units depends on the exact scale factor chosen (see below), but typically unit mass is $1.1 \times 10^{11}\ M_\odot$, unit distance is 10 kpc, and unit time is 50 Myr. A fixed time step Δt of 0.007 time units is used to update the gravitational forces, which are calculated including quadrupole moments in cell interactions and a critical opening angle $\theta = 1$. The softening length for the gravitational force differs depending on the type of particle in question: the stellar particles employ a softening length $\epsilon = 0.02$, while the particles representing gas clouds employ a softening length $\epsilon = 0.04$. The difference in softening length is used to help relieve the perturbing effects of close encounters between the massive stellar particles and the lighter ISM gas clouds. The combined effects of cloud fragmentation and close encounters between the cloud particles and massive stellar particles leads to a relatively large ISM velocity dispersion of $\sigma_v \sim 20\%$ of v_{circ}, which may lead to a "washing out" of very small scale structure that could arise during galaxy interactions. Models with significantly larger number of particles (i.e., an increase by one to two orders of magnitude) would increase the resolution of the simulations and help alleviate this problem, but at a great cost in computing time.

To reduce the amount of model fitting that must be done, each galaxy is assumed to be homologous to the galaxy models described above, aside from a scale factor. The parameters which describe the interaction kinematics include the mass ratio of the two galaxies, the relative orbit of the interaction, and the orientation of the rotational angular momentum vector of each disk. To match an observed system, additional parameters come into play: the line-of-sight direction to the observer and the stage of the interaction (see Fig. 1). A complete search through all available parameter space is clearly prohibitive, so a number of techniques and assumptions are made to narrow this search. In three of the interactions modeled here (NGC 4038/39, NGC 4676, and NGC 7252), the orbital parameters are taken largely or in part from published orbital solutions. The orbital solutions for the remaining two systems presented (IC 1908 and NGC 6872/IC 4970) are original solutions derived here. In each case, the observed morphology and velocity field are used to constrain the orbital solution, which is arrived at after a detailed model matching process involving intuition, assumption, and trial and error.

The first step in determining the interaction parameters is to compare the system morphology to a wide range of models with differing interaction parameters (e.g., Toomre & Toomre 1972, hereafter TT). Once a suitable starting point in parameter space is determined, trial simulations are run to further constrain the orbital parameters. Restricted three-body, or "test particle," simulations are used to quickly survey a range of interactions and are effective at reproducing the morphology and kinematics of the tidal features. These simple models help constrain parameters such as the disk orientations, the correct viewing angles, and stage of the interaction. Following the test particle simulations, small ($N = 4000$) trial N-body simulations are run, which further constrain the models

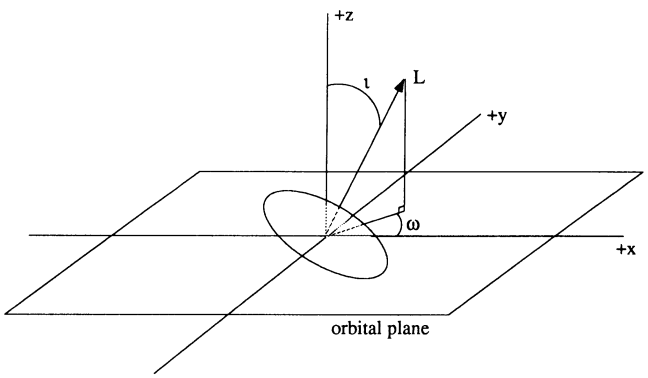

FIG. 1*a*

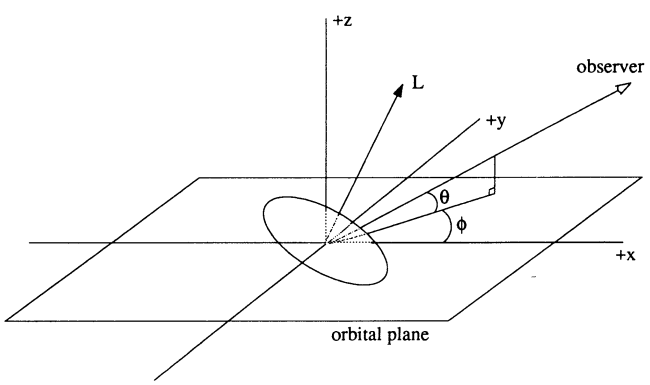

FIG. 1*b*

FIG. 1.—(*a*) Galaxy orientation angles. (*b*) Galaxy observing angles.

through a better modeling of the relative orbit and inner disk morphology. Once a final solution is selected, a few large ($N = 16{,}000$) N-body simulations are used to confirm the accuracy of the best-fit solution.

The final step in the modeling process is to determine the scale factor to apply to the model units to best represent the observed properties of the system. The scaling is done relative to three observed quantities: the gas or total mass of the system, the rotation velocity of the disk or expansion velocity of the tidal tails, and the linear separation of the galaxy pair or extent of the tidal tails. The three scale factors used to transform model units into physical units are not independent, because of (*a*) the gravitational constraint that GM/RV_c^2 must equal one in any set of units, and (*b*) the desire for all model galaxies to have initially identical star formation efficiencies, as measured by the gas depletion time. These two constraints reduce the number of independent fitting parameters to one, which is then chosen to minimize the differences between the observed and modeled properties.

Once calculated, the scaled properties of each model system are compared to the observed properties. This comparison necessarily becomes somewhat coarse due to uncertainties in distant-dependent parameters (we assume $H_0 = 100$ km s^{-1} Mpc^{-1} and small peculiar velocities throughout). Further variables such as the mass-to-light ratio and gas mass fractions compound the problem of obtaining accurate scaling factors. Hence, our comparative analysis will focus on distant independent quantities, such as the relative SFR or the distribution of Hα-emitting gas.

3. NEW OBSERVATIONS OF INTERACTING SYSTEMS

3.1. Hα *Imaging and Long-Slit Spectral Observations: NGC 4676*

The Hα imaging of NGC 4676 was done on 1991 April 4 and 6, at the Michigan-Dartmouth-MIT Observatory (MDM) using the McGraw 1.3 m telescope and Thomson CCD with the MDM broad band filter set and Kitt Peak Hα filter set B. This instrumental setup gave a pixel scale of 0.″48 pixel^{-1}, which was more than adequate for a seeing of $\sim$2″ FWHM. For the R image, one exposure of 900 s was taken, while for the Hα images five on-band and five off-band exposures were taken of 720 s each, in order to eliminate contamination from cosmic rays. The Hα images were calibrated using observations of IRS and Massey et al. (1988) standard stars. The reduction of the images using IRAF[3] consisted of bias-subtracting, flat-fielding, and sky-subtracting each image, then combining the Hα images together into one on- and one off-band image using a median filter.

To determine the velocity field of NGC 4676, long-slit spectral observations were performed at the MDM Observatory on the night of 1990 March 1. The Hiltner 2.4 m telescope was used with the Mk III spectrograph and TI-4849 CCD (Luppino 1989). A 600 lines mm^{-1} grism was used, blazed at $\sim$5900 Å, giving a spectral coverage of $\lambda\lambda$5070–7050. This wavelength range was sufficient to include Hα, [N II] $\lambda\lambda$6548, 6583, and, if strong enough to be detected, [S II] $\lambda\lambda$6717, 6731. The observations were done through a 1.″7 slit, giving a spectral resolution of $\sim$5 Å FWHM. Two slit positions were chosen—one oriented N–S through the major axis and tail of NGC 4676A, and one oriented NE–SW through the major axis of NGC 4676B. To yield the best wavelength fit to the resulting spectra, neon calibration arcs were taken immediately before and after each exposure.

The spectra were reduced using IRAF to perform the bias subtraction, flat-fielding, and two-dimensional wavelength calibration. At this stage, one-dimensional spectra were extracted from the two-dimensional spectral images, and the FIGARO analysis package was used to determine the velocity solution for the emission line system. To determine the uncertainty associated with the velocity solution, artificial spectra were created to match the resolution of the observed spectra, with differing values of signal-to-noise ratio. For S/N = 30–50, a typical value for the observations in the galaxy bodies, the typical error in the fit was $\sim$5 km s^{-1}, while for S/N = 5–10, typical values for observations in the tidal tails, the error was $\sim$15–20 km s^{-1}. Our R-band and Hα images are shown in Figure 2, while the two observed velocity cuts are shown in Figure 3.

3.2. *Fabry-Perot Observations: IC 1908 and NGC 6872/IC 4970*

Clearly, two-dimensional imaging of galaxian velocity fields provide the best basis of comparison to models and avoid many of the problems associated with single-slit observations. Hence, we observed IC 1908 and NGC 6872/IC 4970 on the night of 1990 September 29, using the Rutgers Imaging Fabry-Perot on the 1.5 m telescope at the Cerro Tololo Inter-American Observatory (CTIO). The Fabry-Perot etalons have a FWHM bandpass of 2.3 Å, giving an instrumental dispersion of $\sim$50 km s^{-1} (Schommer et al. 1988). The wavelength scanning was achieved by changing the etalon spacing. To isolate the Hα transmission order, a narrow-band ($\sim$80 Å) Hα filter was used. Using the Tek No. 4 CCD, the instrumental setup gave a circular field of view $\sim$7.′3 in diameter, with a pixel scale of 1.″09 pixel^{-1}—adequate for the seeing, which was $\sim$2.″5 FWHM. IC 1908 was scanned in 12 10 minute exposures, from 7950 km s^{-1} to 8650 km s^{-1} in 45 km s^{-1} steps, while NGC 6872/IC 4970 was scanned in 20 10 minute exposures from 4160 km s^{-1} to 5300 km s^{-1} in 45 km s^{-1} steps.

The raw data images were trimmed, bias-subtracted, flat-fielded, and sky-subtracted. At this stage, the images were shifted to a common centroid, using the stars in the frame as reference points. Shifts were typically less than 1″ over a 2 hr run. To account for changes in sky transparency and airmass over the run, the images were then scaled to a common transparency. This scaling was achieved by performing photometry on relatively bright stars in the field of view, then requiring those stars to have a flat spectrum over the 15 Å baseline scanned. These scaling factors amounted to less than a 10% correction, with a typical uncertainty of $\sim$5%.

To calibrate the wavelength solution for the images, calibration exposures of a neon arc lamp were taken several times during the run. Due to the angular dispersion of the Fabry-Perot, the images are not strictly monochromatic; the wavelength solution varies over an image, with each pixel having a solution which depends on the radial distance r from the optical axis:

$$\lambda = \lambda_0 \cos [\arctan (r/C)] ,$$

where λ_0 represents the central wavelength on the Fabry-Perot optical axis. Therefore, the Ne λ6717 line in each calibration lamp image appears as a ring on the CCD, and the radius and

[3] The Image Reduction and Analysis Facility (IRAF) is distributed by the Association of Universities for Research in Astronomy, Inc., under contract to the National Science Foundation.

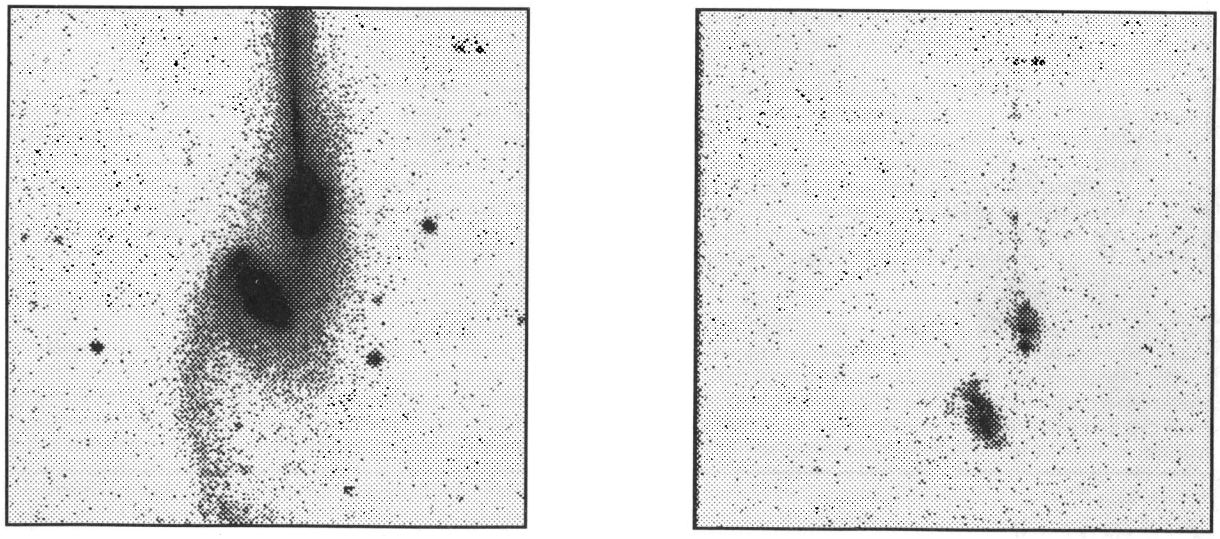

FIG. 2.—NGC 4676. (*a*) *R* band image. (*b*) Hα image. To best show faint detail, both images are scaled logarithmically. North is up, east is to the left.

width of these rings were used to fit the wavelength solution as a function of *r* and etalon spacing.

Once the data processing was done, each pixel in the image had a 12- or 20-point spectrum associated with it, from which four pieces of data were extracted: the continuum intensity, the Hα peak intensity, the radial velocity, and the velocity dispersion. The values were obtained by fitting a Gaussian form to each spectrum and extracting the parameters of the best-fit Gaussian. In regions of low signal, the pixels were binned 3 × 3 to improve the signal and quality of fit. Typical errors in the fit velocity were less than 10 km s^{-1}.

The continuum and Hα intensity maps for IC 1908 are shown in Figure 4, while the velocity and velocity dispersion maps are shown in Figure 5. The continuum and Hα intensity maps for NGC 6872/IC 4970 are shown in Figure 6 and the velocity and velocity dispersion maps are shown in Figure 7. Unlike the situation for IC 1908, the distribution of Hα intensity in the NGC 6872/IC 4970 system traces the continuum light very poorly. In fact, no Hα was detected from IC 4970, perhaps not surprising given its S0 classification. Furthermore, the bar and nuclear regions of NGC 6872 show almost no Hα emission, whereas Hα is observed in the tails, even out where the continuum light has become very diffuse. As a result, the reduced continuum map, derived only in regions where there is observed Hα emission, is a poor representation of the continuum light. For this reason, the continuum map displayed in Figure 6 is a median of all the original exposures, rather than the continuum fit to the Hα emission, and is more correctly an Hα plus continuum map.

3.3. *Determining Star Formation Rates*

In general, star formation rates in external galaxies can be determined either via total Hα luminosity or far-infrared luminosity (see Hunter et al. 1986 for a discussion of both methods).

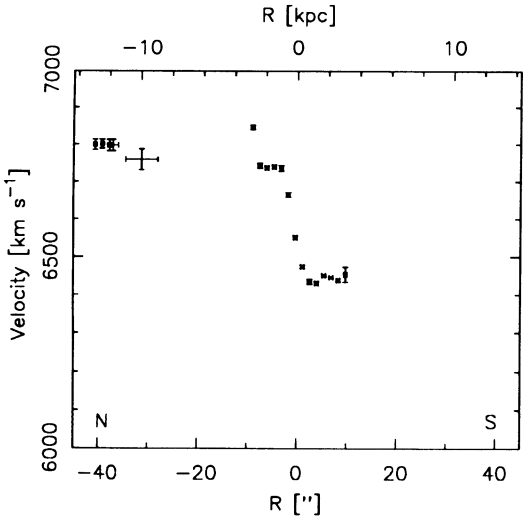

FIG. 3*a*

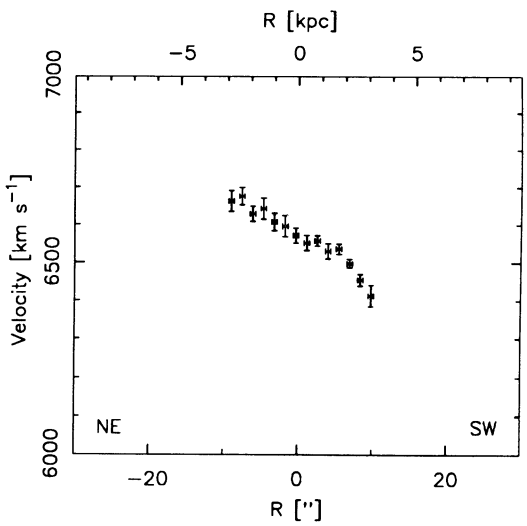

FIG. 3*b*

FIG. 3.—NGC 4676 velocity field. (*a*) N–S slit running through NGC 4676A and tail. (*b*) NE–SW slit running through major axis of NGC 4676B.

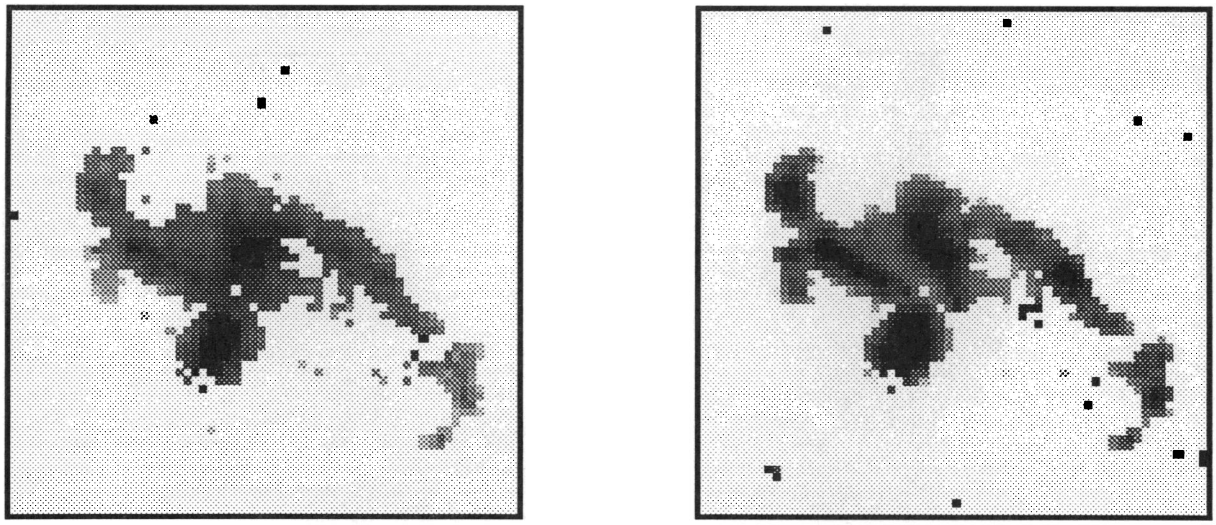

FIG. 4.—IC 1908. (*a*) Continuum map. (*b*) Hα intensity map. To best show faint detail, both images are scaled logarithmically.

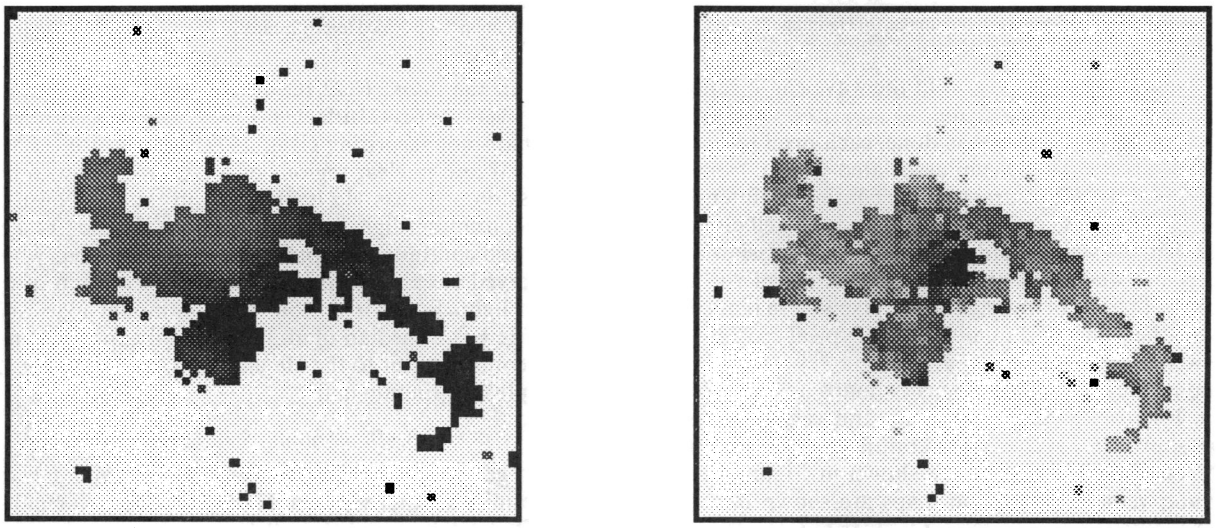

FIG. 5.—IC 1908. (*a*) Velocity map. Dark shading is redshifted, light shading is blueshifted. (*b*) Velocity dispersion map. Darker shading represents higher velocity dispersion.

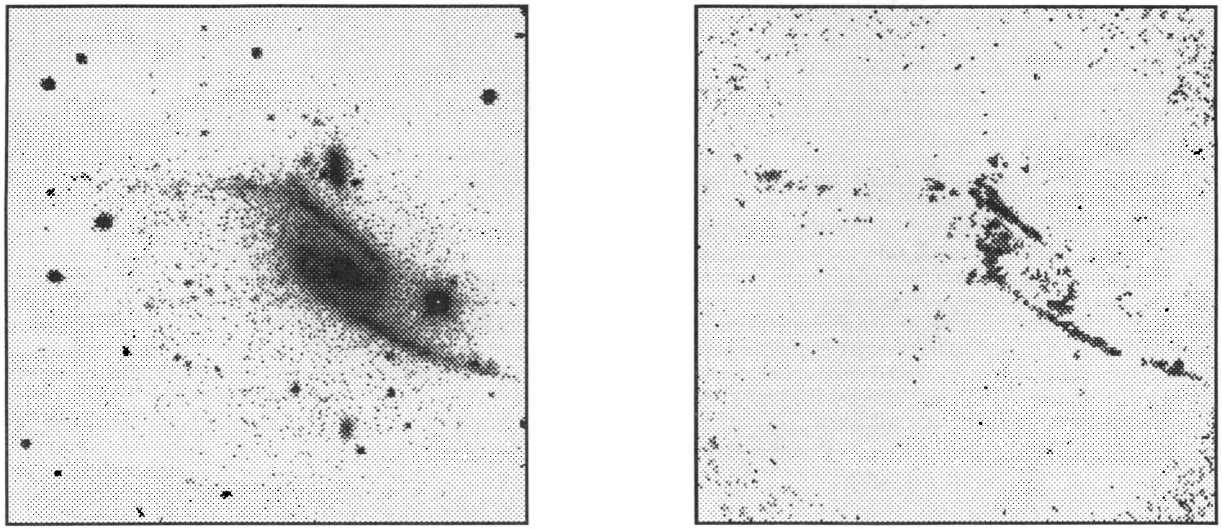

FIG. 6.—NGC 6872/IC 4970. (*a*) Continuum map. (*b*) Hα intensity map. To best show faint detail, both images are scaled logarithmically. North is up, east is to the left.

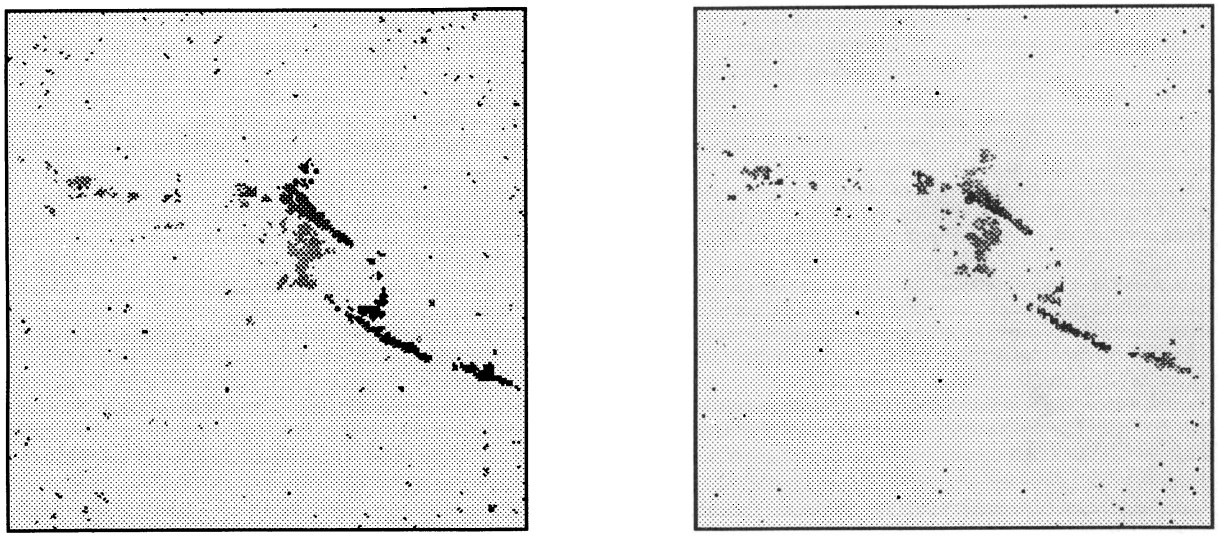

FIG. 7.—NGC 6872/IC 4970. (*a*) Velocity map. Dark shading is redshifted; light shading is blueshifted. (*b*) Velocity dispersion map. Darker shading represents higher velocity dispersion.

In the cases where we have reliable Hα fluxes (e.g., NGC 4676) they were converted into star formation rates using the prescription of Hunter et al. (1986). The derivation of star formation rates from the far-infrared luminosity assumes that the dust heating which gives rise to the far-infrared emission is dominated by UV radiation from massive young stars. To test this assumption, we follow the technique used by Bothun, Lonsdale, & Rice (1989), who point out that a useful indicator of the source of the dust heating is the 60 μm–to–100 μm flux density ratio (f_{60}/f_{100}), a measure of the dust temperature. A value of $f_{60}/f_{100} < 0.3$ is indicative of dust heating dominated by the diffuse interstellar radiation field of old disk stars. As the amount of dust heating by hot, young stars increases, the ratio f_{60}/f_{100} rises as well, until at values of $f_{60}/f_{100} \geq 0.5$ dust heating is entirely dominated by the UV radiation from young stars. Therefore, star formation rates derived from far-infrared luminosities are most valid for galaxies with $f_{60}/f_{100} \geq 0.5$. Table 1 summarizes the *IRAS* properties of each of the five galaxies modeled here, along with the inferred dust temperatures (derived from Helou et al. 1988). All galaxies satisfy $f_{60}/f_{100} \geq 0.5$ except for NGC 6872 which has an extremely low value of f_{60}/f_{100}. Therefore, it is reasonable to assume that in all but NGC 6872, dust heating is dominated by newly formed stars, so that the prescription outlined above to calculate star formation rates is acceptable. The FIR-derived star formation rate for NGC 6872 most probably overestimates the true star formation rate, and is therefore considered an upper limit.

TABLE 1

IRAS PROPERTIES OF MODELED GALAXIES

Galaxy	f_{60} (Jy)	f_{100} (Jy)	f_{60}/f_{100}	T_{dust} (K)
NGC 4038/39	38.9	74.7	0.52	37
NGC 4676	2.56	4.62	0.55	38
IC 1908	3.47	5.72	0.61	40
NGC 6872/IC 4970	1.57	7.23	0.21	26
NGC 7252	4.08	7.08	0.57	39

4. RESULTS

4.1. *NGC 4038/39*

The first galaxy pair modeled is NGC 4038/39 (=Arp 244, VV 245), known commonly as "The Antennae." One of the closest interacting systems, NGC 4038/39 has been well studied at many wavelengths, making it an excellent candidate for the modeling process. Table 2 details the observational properties of NGC 4038/39 in comparison to the best-fit model.

The orbital solution used here is the solution originally derived by TT and adapted to *N*-body parameters by Barnes (1988), and is detailed in Table 3. The model interaction involves two identical galaxies on an elliptical orbit, with an eccentricity of 0.5 and semimajor axis of 3.0 model units. This

TABLE 2

NGC 4038/39 PROPERTIES

Property	Observed	Modeled	Notes
R.A. (2000.0)	$12^h01^m53^s$	...	1
Decl. (2000.0)	$-18°52'30''$	...	1
Heliocentric redshift	1624 km s^{-1}	...	1
Distance	20 Mpc	...	2
M_B	−21.3	...	3
Mass	$2.4 \times 10^{11}\ M_\odot$	$1.8 \times 10^{11}\ M_\odot$	3
Separation	6.6 kpc	8.1 kpc	4
ΔV_{tails}	100 km s^{-1}	110 km s^{-1}	5
ΔV_{disks}	<50 km s^{-1}	55 km s^{-1}	6
Gas mass (total)	$6.3 \times 10^9\ M_\odot$	$5.9 \times 10^9\ M_\odot$	7
Gas mass (disks)	$3.2 \times 10^9\ M_\odot$	$4.6 \times 10^9\ M_\odot$	7
Gas mass (tails)	$3.1 \times 10^9\ M_\odot$	$1.3 \times 10^9\ M_\odot$	7
SFR (4038 nuc; Hα)	$2.1\ M_\odot$ yr^{-1}	$2.7\ M_\odot$ yr^{-1}	8
SFR (4039 nuc; Hα)	$1.7\ M_\odot$ yr^{-1}	$2.7\ M_\odot$ yr^{-1}	8
SFR (overlap; Hα)	$5.0\ M_\odot$ yr^{-1}	$0.03\ M_\odot$ yr^{-1}	8
SFR (combined; FIR)	$14.1\ M_\odot$ yr^{-1}	$5.4\ M_\odot$ yr^{-1}	9

NOTES.—(1) From RC3. (2) Distance interpolated from Aaronson et al. 1982. (3) $M_B = m_B + 5 - 5 \log (D)$, where $m_B = 10.2$ (RC3). (4) Derived using $(M/L)_B = 5\ M_\odot/L_\odot$. (5) From van der Hulst 1979. (6) From Stanford et al. 1990. (7) From van der Hulst 1979 and Stanford et al. 1990. (8) From Stanford et al. 1990. (9) FIR flux from Cataloged Galaxies and Quasars Observed in the *IRAS* Survey 1985; conversion to SFR from Hunter et al. 1986.

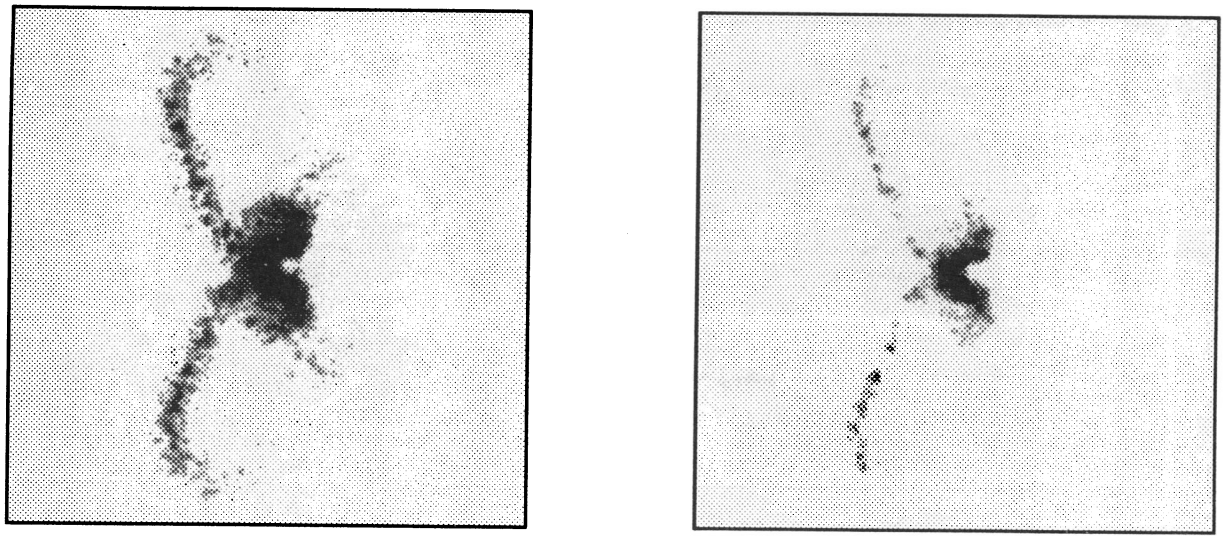

FIG. 8.—NGC 4038/39 model. (*a*) Stellar mass. (*b*) SFR map. To best show faint detail, both images are scaled logarithmically. North is up, east is to the left.

orbit leads to a periapse separation of 1.5 model units at $T = 0$. The encounter is symmetric, with each galaxy inclined 60° to the orbital plane and the system viewed directly along the orbital plane. At the current model time, the disks have already passed the initial periapse 210 Myr ago, and are on the verge of merging, which will take place in ~100 Myr. Images of the NGC 4038/39 model are presented in Figure 8, while the model velocity field is shown in Figure 9.

The morphology of the disks and tails is reproduced reasonably well, with the tails displaying the opposite relative velocity revealed by the H I observations of van der Hulst (1979). The main kinematical objection to this model is the large relative velocity between the two disks. To match the small observed velocity difference between the disks, the observing angles must be changed so greatly that the tails no longer appear crossed, or the time of observation must be delayed—by which time the disks are no longer separate entities. A second problem arises because of the observed disparity between the lengths and masses of the two tails. While NGC 4039's tail is nearly twice as long and contains nearly 4 times as much H I as that of its companion (van der Hulst 1979), the model presents symmetric tails due to the symmetry of the encounter parameters. As pointed out by both TT and van der Hulst, slight differences in the mass ratio or disk inclinations may serve to correct this flaw. The fact that H I and CO observations show that fully half the gas mass in the NGC 4038/39 system lies in the tails (van der Hulst 1979; Stanford et al. 1990), while only 25% of the gas in the model lies in the tails, suggests another possible improvement to this model: the initial distribution of ISM gas in the system may have been more extended than the distribution used in the models, resulting in more gas being included in the tidal tails, and less gas remaining behind in the interacting disks.

In order to evaluate how a more extended distribution of gas effects the model results, we ran an interaction in which the gas disks of each galaxy were extended out 40% further in radius, effectively doubling the gas mass of each galaxy. Examining the resultant models, we find that the gas distribution is now divided equally between the disks and the tails, in better agreement with the observed H I and CO distributions. However, by altering the gas distribution of the progenitor galaxies to best fit the observed parameters we are trying to address, namely the current gas distribution and star formation rates, we run the risk of correctly selecting from a continuum of possible answers simply through a advantageous choice of input

TABLE 3

NGC 4038/39 ORBIT

Parameter	Model Units	Scaled Units
Mass ratio	1:1	...
Orbit	Elliptical	...
Eccentricity	0.5	...
Semi-major axis	3	27.3 kpc
NGC 4038 orientation	(60°, 240°)	...
NGC 4039 orientation	(60°, 60°)	...
Viewing angle	(0°, 150°)	...
Viewing time	4.2	210 Myr

FIG. 9.—NGC 4038/39 model velocity field. Dark shading is redshifted; light shading is blueshifted.

parameters. Since we are more interested in how a *typical* galaxy would respond to the gravitational encounter, we choose to focus our analysis on the models with the standard gas disk. This choice also allows for a better intercomparison between the results from each modeled encounter, since all progenitor galaxies will be identical.

We can also compare the observed distribution of Hα and CO to the spatial distribution of star formation in the model. Stanford et al. (1990) derive Hα-based and 10 μm emission–based star formation rates of 2.1 $M_\odot$ yr^{-1} and 1.7 $M_\odot$ yr^{-1} for the nuclear regions of NGC 4038 and NGC 4039, respectively, and a star formation rate of 5 $M_\odot$ yr^{-1} for the region where the disks overlap. The amount of CO associated with these regions is 8.3×10^8 $M_\odot$, 2.4×10^8 $M_\odot$, and 12.0×10^8 $M_\odot$, respectively. Examining similarly chosen regions in the model, star formation rates of 2.7 $M_\odot$ yr^{-1}, 2.6 $M_\odot$ yr^{-1}, and 0.03 $M_\odot$ yr^{-1} are found, with corresponding gas masses of 6.7, 6.7, and 4.0×10^8 $M_\odot$. Therefore, while the models predict that the nuclear regions should carry the vast majority of the star formation and ISM mass in this system, observations reveal that the SFR and CO emission are fairly evenly divided between the nuclear and overlap regions.

Two possible explanations for this discrepancy are considered here. First, the overlap region may be forming stars with a much higher efficiency than the nuclear regions. Several authors have proposed that star formation induced by cloud collisions in the disturbed ISM may trigger the copious star formation rates seen in several interacting systems (Scoville, Sanders, & Clemens 1986). This mechanism may be most important in the outer portions of the disk which have directly collided, driving a higher efficiency of star formation. However, the gas depletion timescales for the three regions are comparable. A second explanation for this discrepancy lies in the differing spatial distributions of gas. The observations show that the overlap region harbors more gas than the nuclei do; this result is opposite to the sense of the models. Therefore it is likely that the failure of the model to reproduce the large quantity of overlap gas is the reason that relatively little star formation is modeled there. Physically the observations may reflect an ISM that is more viscous than that represented in the models, such that a larger quantity of gas builds up in the region where the disks are in contact and is less able to fall into the nuclear regions.

The overall modeled history of star formation in NGC 4038/39 is presented in Figure 10. The present SFR is approximately 5 times the preencounter rate, and the nuclear starbursts are fading as star formation depletes the nuclear gas. However, with the galaxies set to merge, the star formation rate is boosted again in ~100 Myr, at which point the galaxies have merged and the star formation history is governed by gas depletion via the nuclear burst. The maximum increase in the star formation rate comes just after the galaxies merge and is only a factor of ~6. This relatively mild burst of star formation accompanying the merger (compared to the mergers modeled in MRB) is a result of the highly inclined nature of the interaction, which lessens the effectiveness of triggering radial gas flows, and the wide orbit, which delays the merging and gives the starbursts more time to deplete the gas supply. Therefore even at the stage when this system merges, the model predicts that NGC 4038/39 will not join the ranks of the ultraluminous infrared galaxies.

4.2. *NGC 4676*

The next galaxy pair modeled is NGC 4676 (=Arp 242, VV 224), commonly known as "The Mice." The observational properties of NGC 4676 are given in Table 4. The orbital solution is based on the solution presented by TT, with slight modifications, and is shown in Table 5. The interaction involves two identical galaxies on an elliptical orbit of eccentricity 0.6 and semimajor axis of 4 model units, bringing it to periapse separation of 1.6 model units at $T = 0$. NGC 4676A is on a prograde orbit, with its disk inclined only 15° to the orbital plane, while NGC 4676B is on a more highly inclined orbit, tilted 60° away from the orbital plane. The galaxies are viewed only 10° above the orbital plane, such that NGC 4676A is seen nearly edge-on, displaying a very thin, linear tidal tail. The viewing time is $T = 3.6$, or 180 Myr after periapse. This viewing time is ~100 Myr earlier than that proposed by TT but is chosen to better fit the separation of the galaxies and the position axis of NGC 4676B's major axis. At a later time, the galaxies are too close and the PA of NGC 4676B has rotated 90° out of alignment. The main complaint with the model presented here is that the model tidal tails are ~50% shorter than the observed tails; however, this discrepancy could probably be rectified by a model with more extended disks or a somewhat slower orbit. Images of the best fit model of NGC

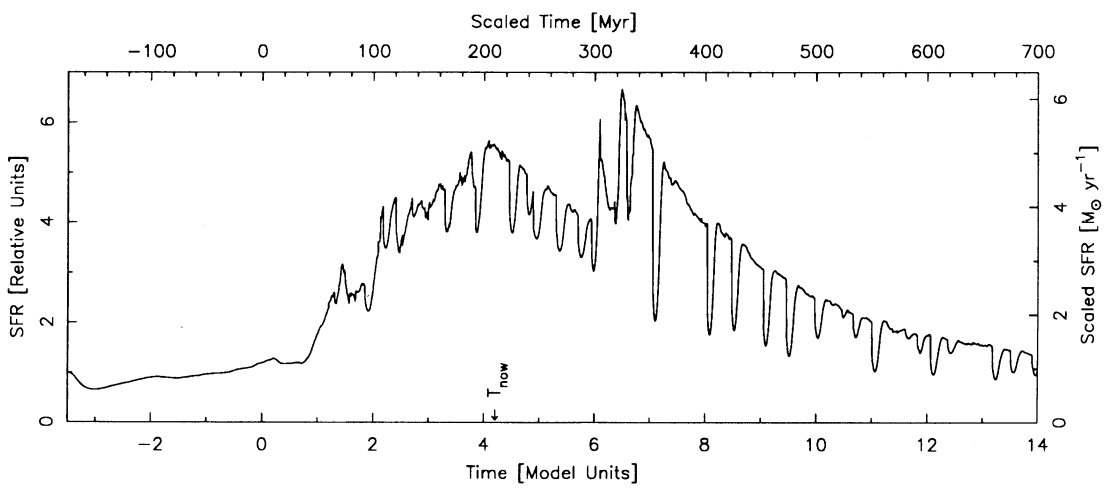

FIG. 10.—NGC 4038/39 model SFR evolution. Present time is denoted as T_{now}.

TABLE 4

NGC 4676 PROPERTIES

Property	Observed	Modeled	Notes
R.A. (2000.0)	$12^h46^m11^s$	...	1
Decl. (2000.0)	+30°43′45″	...	1
Heliocentric redshift	6600 km s^{-1}	...	1
Distance	63 Mpc	...	2
M_B	−20.0	...	3
Mass	$8 \times 10^{10}\ M_\odot$	$8.6 \times 10^{10}\ M_\odot$	4
Separation	11.1 kpc	14.3 kpc	5
$\Delta V_{\rm Atail}$	150 km s^{-1}	115 km s^{-1}	5
$\Delta V_{\rm disks}$	100 km s^{-1}	115 km s^{-1}	5
Gas mass (4676A)	$1.7 \times 10^9\ M_\odot$	$1.3 \times 10^9\ M_\odot$	6
Gas mass (4676B)	$1.5 \times 10^9\ M_\odot$	$1.7 \times 10^9\ M_\odot$	6
SFR (4676A; Hα)	$0.8\ M_\odot$ yr^{-1}	$2.9\ M_\odot$ yr^{-1}	5, 7
SFR (4676B; Hα)	$1.7\ M_\odot$ yr^{-1}	$0.8\ M_\odot$ yr^{-1}	5, 7
SFR (combined; FIR)	$8.8\ M_\odot$ yr^{-1}	$3.7\ M_\odot$ yr^{-1}	8

NOTES.—(1) From RC3. (2) Distance = cz/H_0, with a Virgocentric flow of 300 km s^{-1}. (3) $M_B = m_B + 5 - 5 \log (d)$, where $m_B = 14.0$ (Bushouse 1987). (4) Derived using $(M/L)_B = 5\ M_\odot/L_\odot$. (5) This work. (6) From Bushouse 1987. (7) Conversion from Hα flux to SFR from Gallagher, Hunter, & Tutukov 1984. (8) FIR flux from Cataloged Galaxies and Quasars Observed in the *IRAS* Survey 1985; conversion to SFR from Hunter et al. 1986.

TABLE 5

NGC 4676 ORBIT

Parameter	Model Units	Scaled Units
Mass ratio	1:1	...
Orbit	Elliptical	...
Eccentricity	0.6	...
Semi-major axis	4	29 kpc
NGC 4676A orientation	(15°, 180°)	...
NGC 4676B orientation	(60°, 0°)	...
Viewing angle	(10°, 0°)	...
Viewing time	3.6	180 Myr

4676 are shown in Figure 11, while Figure 12 shows model velocity cuts chosen to match the observed spectral slits.

A comparison between the observed Hα-deduced star formation rates and the model star formation rates shows that while the model predicts that NGC 4676A should be forming stars at twice the rate of its companion, the opposite is observed to be true. However, the derived star formation rates are fairly suspect in that they do not correct for Hα absorption due to material in the galaxies' disks. This effect may be particularly strong in NGC 4676A, which is observed nearly edge-on, and a correction for internal absorption could bring the observations and model into agreement. Alternatively, the models may overestimate the amount of gas channeled into the nuclear regions of NGC 4676A and thus overestimate the relative strength of the associated starburst. A less massive concentration of nuclear gas could result if NGC 4676A were initially gas poor relative to its companion, or if galaxies are more stable against the growth of the nuclear gas concentrations than are the models shown here.

The evolution of the global SFR in NGC 4676 is shown in Figure 13. At the current time, the models show that the star formation rate in this system has been elevated by a factor of ~8, a burst comparable in strength to the starburst triggered in NGC 4038/39. It is thus comforting to note that the star formation rates in these two systems as evaluated by their far-infrared luminosities—which do not suffer from absorption effects—are comparable, although larger than inferred by the Hα luminosities. Because of the relatively wide orbit, the galaxies take longer to merge than do NGC 4038/39 and are merging only at $T \sim 14$, or ~700 Myr after the initial encounter. By this time, well over half the initial gas mass has been depleted by the induced starbursts, resulting in only a weak merger-induced starburst. Like NGC 4038/39, NGC 4676 will merge without ever becoming ultraluminous.

4.3. *IC 1908*

The southern interacting galaxy pair IC 1908 involves a close encounter between a larger galaxy displaying two strong tidal arms and a smaller, relatively undistorted companion. Table 6 summarizes the observed properties of IC 1908. The orbital solution derived for IC 1908 (Table 7) consists of a pair of galaxies with a mass ratio 2.4:1 traveling on a highly inclined, elliptical orbit. The system is viewed along the orbital plane approximately 100 Myr after closest approach. The main

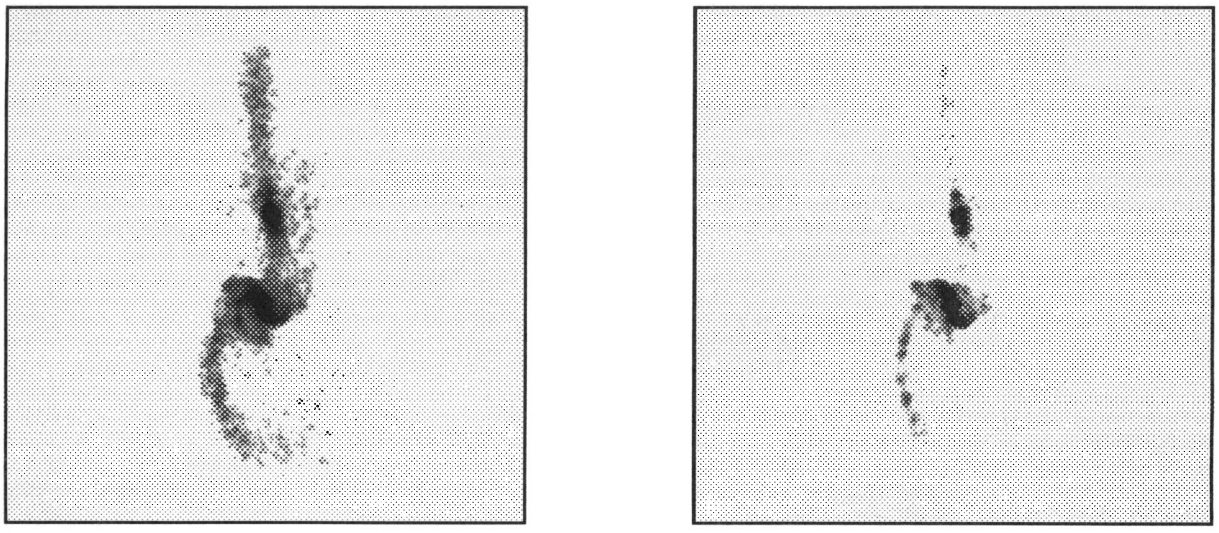

FIG. 11.—NGC 4676 model. (*a*) Stellar mass. (*b*) SFR map. To best show faint detail, both images are scaled logarithmically.

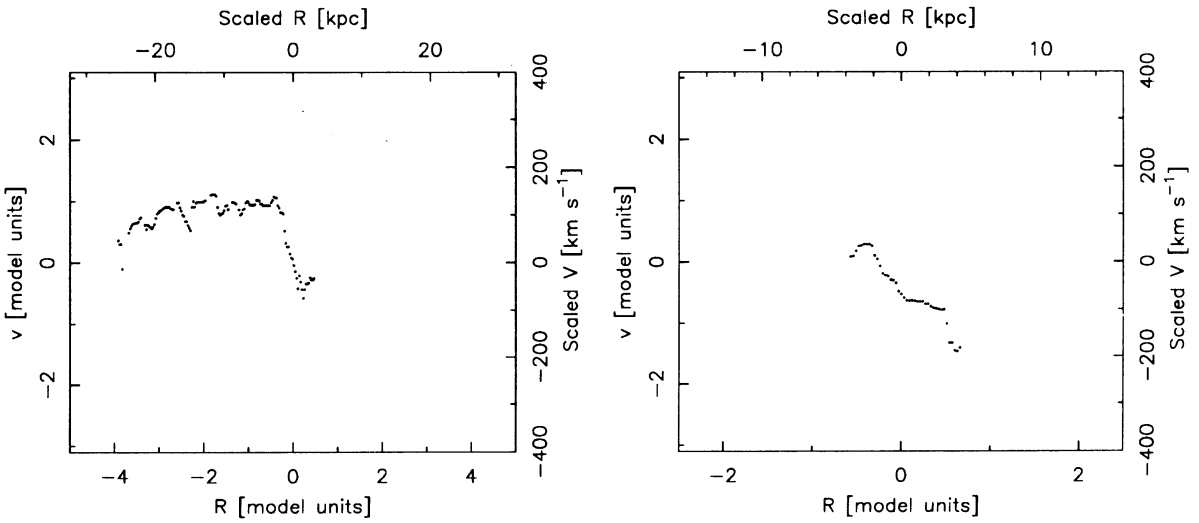

FIG. 12.—NGC 4676 model velocity field. "Slits" chosen to match orientation of the observations.

kinematical objection to this model solution is the high rotation velocity of the companion; this detail could be corrected by using a larger, less dense companion or lowering the inclination of the companion to the line of sight. The stellar mass and star formation maps of the IC 1908 model are shown in Figure 14, while the model velocity field is shown in Figure 15.

The IC 1908 model reproduces several star-forming properties of the system rather well. Star formation in the companion is relatively smooth and unperturbed as a result of the companion's geometry—tilted only 45° away from a purely retrograde encounter. Furthermore, the relative intensity of the star formation in the arms of the primary galaxy corresponds well to the observed distribution. The fact that the eastern arm of

TABLE 6

IC 1908 PROPERTIES

Property	Observed	Modeled	Notes
R.A. (2000.0)	$3^h15^m5^s$	...	1
Decl. (2000.0)	−54°49′3″	...	1
Heliocentric redshift	8439 km s^{-1}	...	1
Distance	84 Mpc	...	2
M_B	−20.3	...	3
Mass	$9.5 \times 10^{10}\ M_\odot$	$8.2 \times 10^{10}\ M_\odot$	4
Separation	4.6 kpc	8.7 kpc	5
ΔV_{prim}	300 km s^{-1}	210 km s^{-1}	5
ΔV_{comp}	150 km s^{-1}	210 km s^{-1}	5
SFR (combined; FIR)	19.6 $M_\odot$ yr^{-1}	0.5 $M_\odot$ yr^{-1}	6

NOTES.—(1) From RC3. (2) Distance = cz/H_0. (3) $M_B = m_B + 5 - 5 \log (d)$, where $m_B = 14.3$ (RC3). (4) Derived using $(M/L)_B = 5\ M_\odot/L_\odot$. (5) This work. (6) FIR flux from Cataloged Galaxies and Quasars Observed in the *IRAS* Survey 1985; conversion to SFR from Hunter et al. 1986.

TABLE 7

IC 1908 ORBIT

Parameter	Model Units	Scaled Units
Mass ratio	2.4:1	...
Orbit	Elliptical	...
Eccentricity	0.7	...
Semi-major axis	1.2	10 kpc
Primary orientation	(100°, 270°)	...
Companion orientation	(135°, 290°)	...
Viewing angle	(5°, 300°)	...
Viewing time	1.9	95 Myr

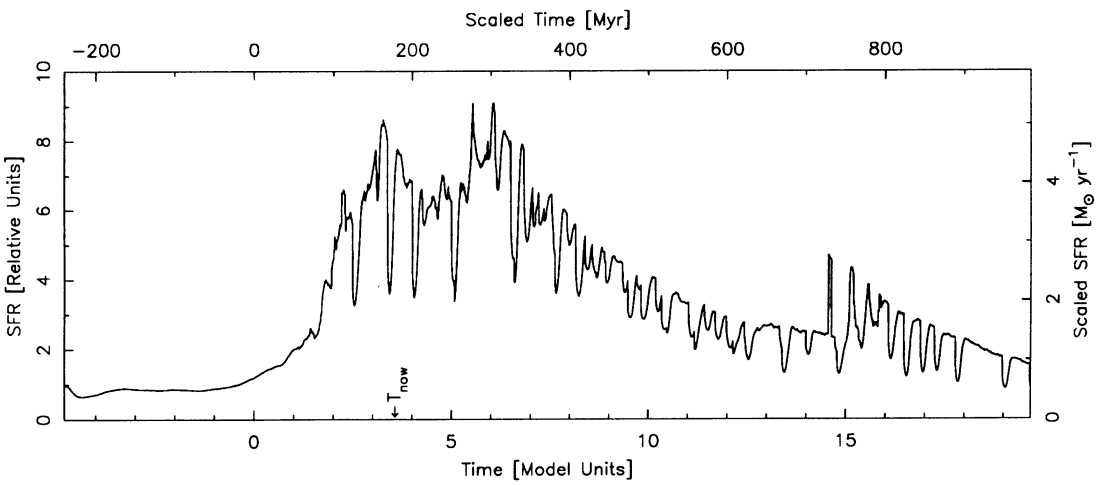

FIG. 13.—NGC 4676 model SFR evolution. Present time is denoted as T_{now}.

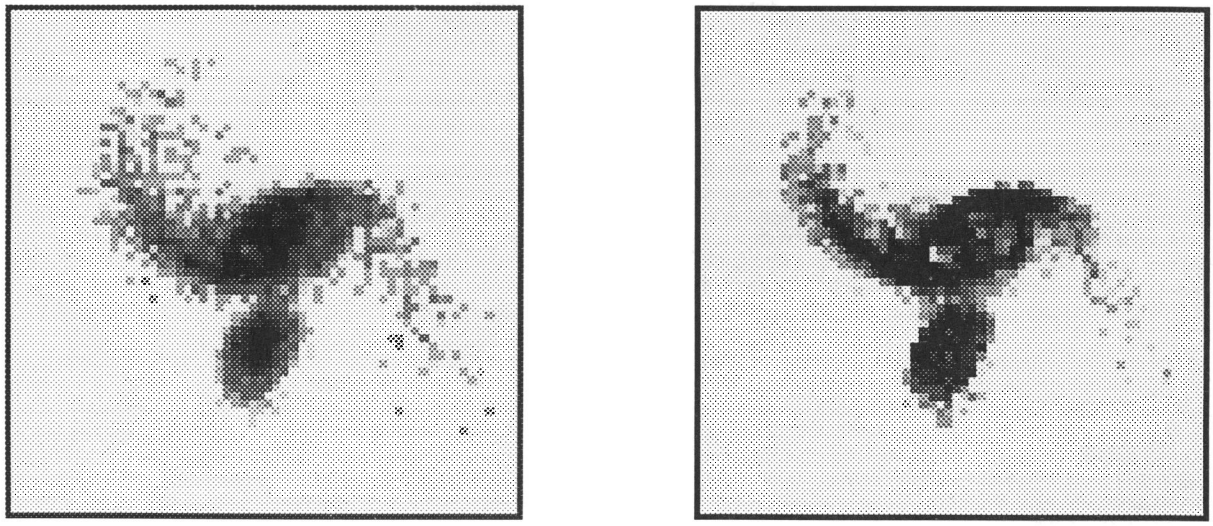

FIG. 14.—IC 1908 model. (*a*) Stellar mass. (*b*) SFR map. To best show faint detail, both images are scaled logarithmically.

IC 1908 has a higher rate of star formation than the western arm is a direct result of the fact that material in the western arm was closest to the companion at periapse. Since the tidal force in a gravitational encounter scales as r^{-3}, this material receives a stronger perturbation than does the material on the opposite side of the disk, and this strong perturbation results in a very dispersed tidal arm. The eastern arm, being further away from the companion, receives a gentler perturbation, which results in compressing, rather than dispersing, the material. However, the models fail to reproduce the clumpiness of the observed star formation, giving a smooth distribution which follows the tidal features. As noted previously, the large ISM velocity dispersion in the galaxy models acts to wash out the small-scale perturbations that could give rise to these clumps; furthermore it is unclear whether such clumpiness is a result of the gravitational encounter or merely reflective of an initially clumpy ISM.

An examination of the modeled evolution of star formation in this system (Fig. 16) yields some interesting conclusions. At the current time, while showing the dramatic tidal disruption, the global star formation rate in this system has not significantly changed from its pre-interaction level. In fact, over the 600 Myr after closest approach, the star formation rate increases only by a factor of 2. This relative inactivity results from the highly inclined orbit the galaxies travel on; although the interaction is sufficiently close enough to form tidal arms which mildly compress the gas, neither mass accretion nor bar formation occurs. As shown in MRB, these two mechanisms are the dominant trigger for starbursts in interacting systems; since neither mechanism occurs in IC 1908, the induced starburst is relatively mild. This result, however, is at odds with the current star formation rate inferred by the observed far-infrared flux. The FIR flux from IC 1908 suggests this system has a star formation rate higher than those observed in either NGC 4038/39 or NGC 4676, and an order of magnitude greater than predicted by the model. Since much of the star formation in this system arises from the clumpy distribution of star formation in the arms, this discrepancy may suggest that the star formation response to mild gravitational encounters is more sensitive to the small-scale perturbations than the overall tidal forces. Such a scenario would represent yet another barrier to successful modeling of global star formation, as the quality of the star formation model would depend critically on the small scale, rather than global, distribution of ISM mass. An alternate—and not so discouraging—explanation for this discrepancy might be that IC 1908 is a very gas rich system, such that the high star formation rate may reflect high preinteraction levels of star formation, boosted mildly by the interaction. If so, the light from IC 1908 should be dominated by relatively young A–F stars from this preinteraction phase; however, the $(B-V)_e$ color of IC 1908 is 0.61 ± 0.03 (RC3), too red for such a population.

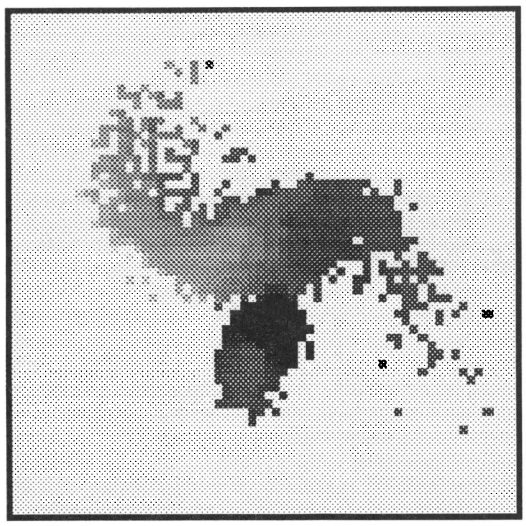

FIG. 15.—IC 1908 model velocity field. Dark shading is redshifted; light shading is blueshifted.

The velocity dispersion information obtained by the Fabry-Perot can also be used to investigate the kinematical environment of the star-forming regions in IC 1908. The relationship between velocity dispersion and star formation rate is an important one in many star formation scenarios. Under "critical density" models (e.g., Kennicutt 1989), star formation results from a gravitational instability which results when the

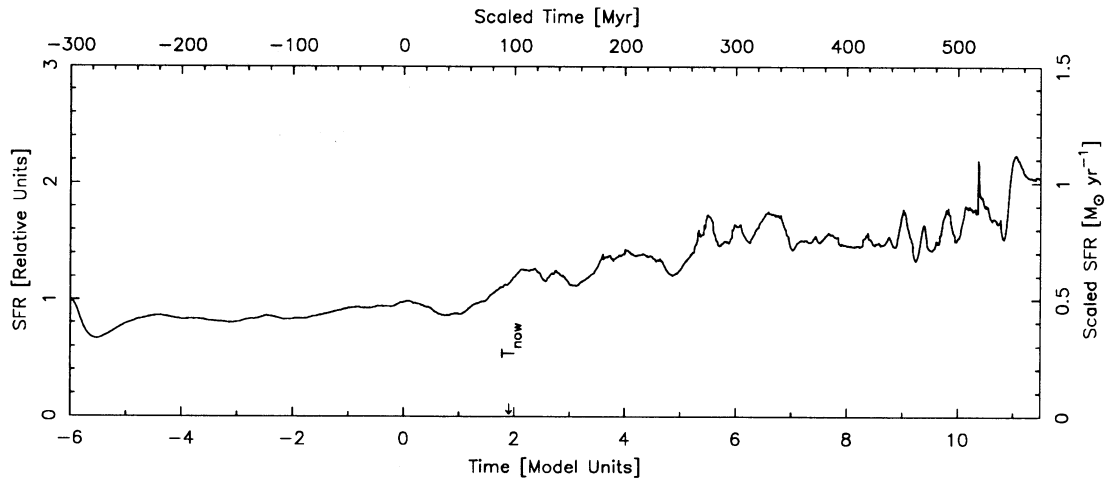

FIG. 16.—IC 1908 model SFR evolution. Present time is denoted as T_{now}.

surface density of gas exceeds a critical defined by the Toomre (1964) instability:

$$\Sigma_{crit} = \alpha \frac{\kappa \sigma_v}{3.36G},$$

where α is a numerical constant ~ 1, G is the gravitational constant, κ is the epicyclic frequency, and σ_v is the velocity dispersion of the gas. Under this scenario, therefore, star formation should be suppressed in regions of high velocity dispersion, unless the gas surface density is very high. Alternately, star formation may occur as a result of cloud collisions in the disturbed ISM (e.g., Scoville et al.). Since the cloud collision rate is proportional to σ_v, regions of high velocity dispersion may have higher rates of star formation. A plot of relative Hα intensity versus velocity dispersion for IC 1908 is presented in Figure 17. While no clear trend can be seen in the data, star formation is occurring even at very high velocity dispersion, which suggests either the star formation has been induced by cloud collisions in the ISM, or that the surface density of gas must be very high in these regions. An alternate interpretation, however, could be that the high velocity dispersion is a result of—rather than the cause of—the high observed star formation rates, as the stellar winds from young OB stars heat the surrounding ISM.

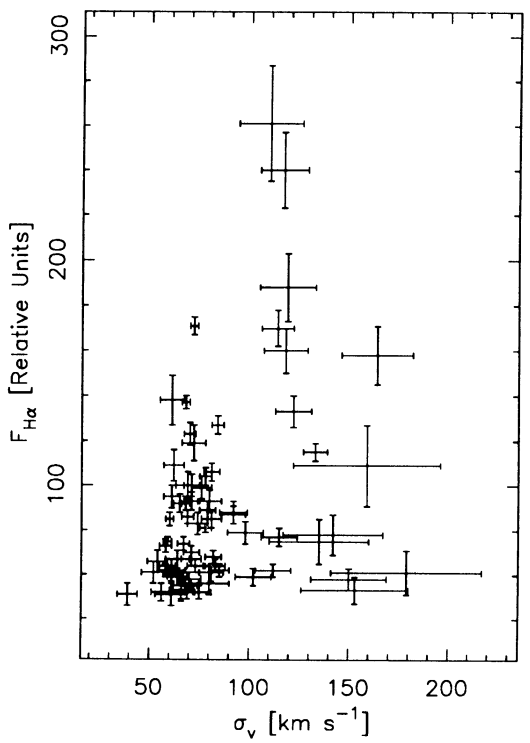

FIG. 17a

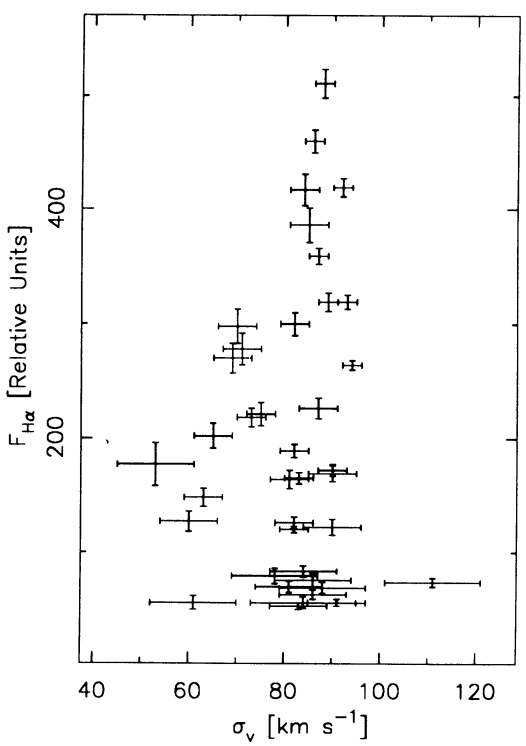

FIG. 17b

FIG. 17.—Hα intensity vs. velocity dispersion in IC 1908. (*a*) Primary galaxy. (*b*) Companion galaxy.

TABLE 8

NGC 6872/IC 4970 PROPERTIES

Property	Observed	Modeled	Notes
R.A. (2000.0)	$20^h16^m56^s$	...	1
Decl. (2000.0)	$-70°46'4''$	...	1
Heliocentric redshift	4701 km s^{-1}	...	1
Distance	47 Mpc	...	2
M_B	−21.9	...	3
Mass	$4.5 \times 10^{11}\ M_\odot$	$5.6 \times 10^{11}\ M_\odot$	4
Separation	13 kpc	21 kpc	5
ΔV_{prim}	850 km s^{-1}	580 km s^{-1}	5
ΔV_{pair}	50 km s^{-1}	130 km s^{-1}	6
M_{gas}	$<2.3 \times 10^9\ M_\odot$	$1.8 \times 10^{10}\ M_\odot$	7
SFR (FIR)	$<5.7\ M_\odot\ yr^{-1}$	$3.7\ M_\odot\ yr^{-1}$	8

NOTES.—(1) From RC3. (2) Distance = cz/H_0. (3) $M_B = m_B + 5 - 5 \log (d)$, where $m_B = 14.7$ (RC3). (4) Derived using $(M/L)_{B,6872} = 5\ M_\odot/L_\odot$ and $(M/L)_{B,4970} = 10\ M_\odot/L_\odot$. (5) This work. (6) From Green et al. 1988. (7) From Reif et al. 1982. (8) FIR flux from Cataloged Galaxies and Quasars Observed in the *IRAS* Survey 1985; conversion to SFR from Hunter et al. 1986.

4.4. *NGC 6872/IC 4970*

The next interacting galaxy pair modeled is NGC 6872, a luminous barred spiral displaying a pair of long, thin tidal arms, and its small companion IC 4970, classified as an S0 in the RC3. This pair is a member of the Pavo group, and lies in a relatively crowded field which includes NGC 6876 and NGC 6877 approximately 8′ distant. At the distance of NGC 6872, taken to be 46 Mpc, NGC 6876/78 lies at least 100 kpc away from NGC 6872, and with a relative velocity of 700 km s^{-1} (Green, Godwin, & Peach 1988), it is assumed that NGC 6876/78 has played little or no role in the dynamics of the NGC 6872/IC 4970 system. The observational properties of the NGC 6872/IC 4970 system are presented in Table 8.

The orbital solution for the NGC 6872/IC 4970 system describes a highly prograde encounter between a large disk galaxy and a smaller companion (Table 9). To determine the mass ratio of the two galaxies, the assumption of similar mass-to-light ratios was used initially, and based on a *B* magnitude difference of 2.8 mag (RC3), the first attempts at modeling this system involved galaxies with a mass ratio of 10:1. The test particle simulations quickly showed this mass ratio was unable to drive the tidal features observed in NGC 6872, so a mass ratio of 5:1 was adopted instead. Given the uncertainties in observed mass-to-light ratios and the fact that the galaxies are of different Hubble types, a factor of 2 difference in the mass-to-light ratio is not surprising. Finally, no ISM clouds are placed in the companion due to its S0 classification. Figure 18 shows the modeled stellar mass distribution and star formation map, while the model velocity field is shown in Figure 19.

TABLE 9

NGC 6872/IC 4970 ORBIT

Parameter	Model Units	Scaled Units
Mass ratio	5:1	...
Orbit	Parabolic	...
R_{peri}	1.2	19 kpc
NGC 6872 orientation	(25°, 315°)	...
IC 4970 orientation	(90°, 0°)	...
Viewing angle	(30°, 115°)	...
Viewing time	2.9	145 Myr

The model reproduces several properties of the encounter well, including the stellar bar, the morphology and extent of the tidal tails, and even the tidal debris near IC 4970, which is due to the stripping of material from NGC 6872 during the close encounter. One problem with the model is the modeled velocity difference between the pair; the radial velocity of IC 4970 (4759 km s^{-1}; Green et al. 1988) is essentially the same as NGC 6872, whereas the model gives IC 4970 a substantial blueshift. A more serious problem with the model, from a star-forming perspective, is the inability of the model to accurately realize the thinness of the tidal features. The high velocity dispersion of the model smears out the tails, limiting the tidal compression of gas and most likely underestimating the induced star formation in the tails.

The most dramatic difference between the observed and modeled star-forming properties of the NGC 6872/IC 4970 system, however, is the spatial distribution of star formation. While the Hα maps show the star formation occurring only

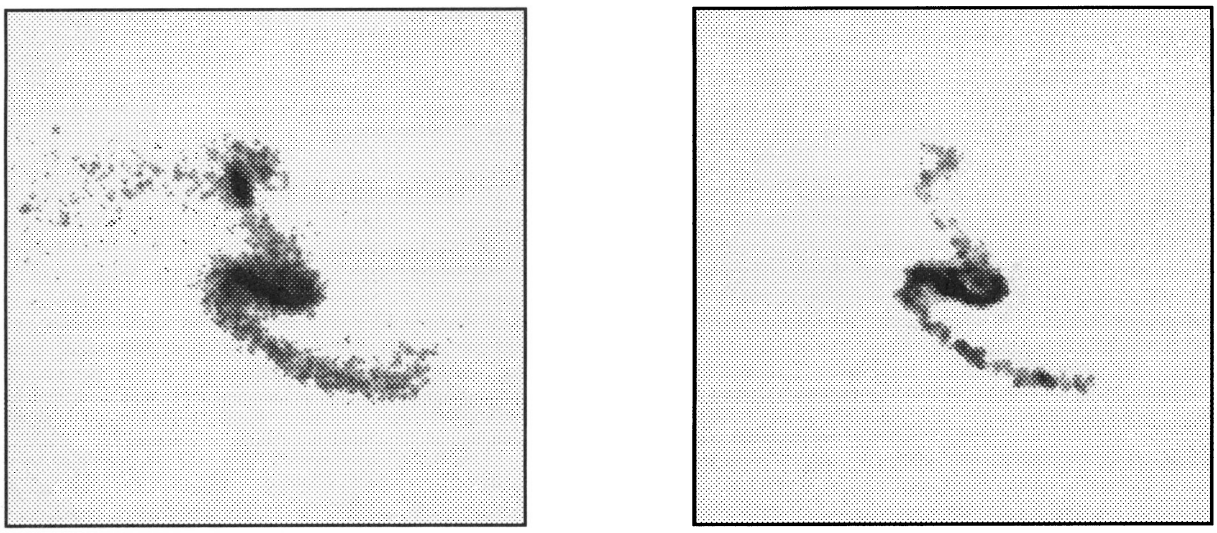

FIG. 18.—NGC 6872/IC 4970 model. (*a*) Stellar mass. (*b*) SFR map. To best show faint detail, both images are scaled logarithmically.

FIG. 19.—NGC 6872/IC 4970 model velocity field. Dark shading is redshifted; light shading is blueshifted.

along the tidal arms, the models display the majority of the star formation in the bar and nuclear regions, as ISM material crowds along the bar and falls toward the nucleus. In fact, the flow of gas triggered by this bar mode is responsible for a doubling of the global SFR in the model in $\sim$100 Myr from the current time (see Fig. 20). Since the formation of a bar is one of the primary triggers of nuclear gas flows and starbursts, the fact that this system shows no star formation interior to the tidal arms represents a surprising deviation from the standard picture of interaction-induced starbursts. However, the probable solution to this discrepancy lies in the very small gas mass fraction of NGC 6872. Observations at 21 cm by Reif et al. (1982) failed to detect H I from NGC 6872, putting an upper limit on the H I mass of $2.3 \times 10^9\ M_\odot$, or a gas mass fraction of $\lesssim$0.4%. It is unlikely that the interaction could have produced a burst of star formation so intense as to deplete the gas mass by an order of magnitude during the relatively short time since closest approach—the star formation rates required to do so would be $\sim 150\ M_\odot\ \mathrm{yr}^{-1}$. It is more likely that NGC 6872 was relatively gas poor to begin with, or that the majority of gas in the system lies at a large radius, such that no central gas flows have occurred.

To evaluate such a scenario, in which NGC 6872 initially had the majority of its gas at large radii, we have rerun the encounter simulation with the gas initially distributed in the radial range $0.6 < R < 1.0$. While the gas distribution has been chosen ad hoc, it is not inconsistent with observations of disk galaxies, which often show radial depressions, or "holes," in their H I and CO distributions (see Young & Scoville 1991). The resultant distribution of gas and star formation in the interaction model is strongest along the tidal features, and shows no tendency to accumulate along the stellar bar. However, we point out that observations of barred galaxies often show star formation to be suppressed in the region of the bar (Phillips 1993), suggesting that the star formation law itself may be different in such environments, perhaps strongly tied to the gasdynamics along the bar (e.g., Tubbs 1982). As in the case of the NGC 4038/39 model, we offer this iteration of the model as one possible improvement, but choose to focus our analysis on the model with a uniform gas disk.

Without the nuclear starburst associated with bar formation, what is the dominant trigger mechanism for the star formation in NGC 6872? Clues can be found by inspecting the velocity and velocity dispersion maps. The regions of highest velocity dispersion are located along the tidal arms, where some of the strongest sites of star formation are found (see Figs. 7 and 21). In fact, the velocity gradient on the southern arm is $\sim 150\ \mathrm{km\ s}^{-1}$ over a 2 kpc cut across the arm. The sense of the gradient is such that material on the back edge of the arm—the northern side—is running into the material on the leading edge of the arm. A similar trend is seen in the northern arm, although not as coherently since this arm received a more dispersive perturbation. The fact that the most intense star formation is found where the gas compressions are strongest argues in favor of collisionally induced star formation being the dominant star-forming mechanism in NGC 6872. Furthermore, given the very high rotation velocity of NGC 6872, the critical gas surface density for star formation to occur under threshold models (Kennicutt 1989) is $\sim 100\ M_\odot\ \mathrm{pc}^{-2}$ at the radius of the tidal arms (assuming a flat rotation curve and preinteraction velocity dispersion of $\sim 20\ \mathrm{km\ s}^{-1}$). In light of the very small upper limit on the H I gas mass of NGC 6872, it seems likely that the gas surface density is much lower than

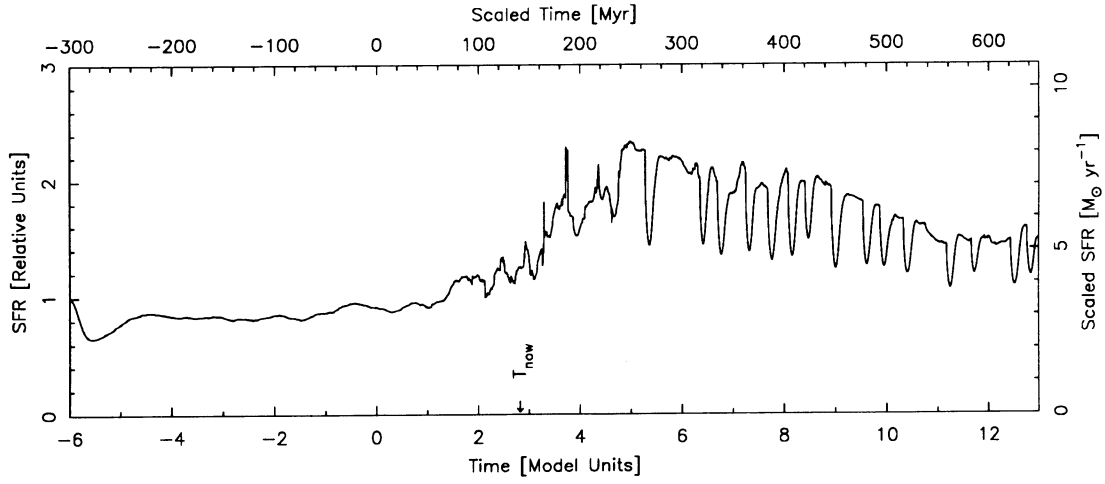

FIG. 20.—NGC 6872/IC 4970 model SFR evolution. Present time is denoted as T_{now}.

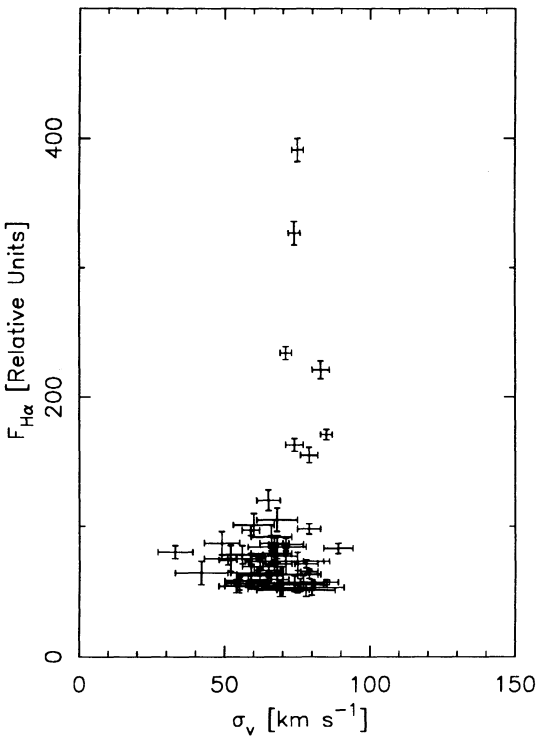

FIG. 21.—Hα intensity vs. velocity dispersion in NGC 6872

this critical density, so that without the collisionally induced star formation triggered by the interaction with IC 4970, NGC 6872 would show little or no star formation at all.

4.5. *NGC 7252*

The final galaxy interaction modeled is NGC 7252 (Arp 226), a probable merger between two disk galaxies and suspected young elliptical (Schweizer 1982). NGC 7252 displays two long tidal tails projecting from a single central body which shows a complex system of loops and ripples, all kinematic signatures of a recent merger. The observed properties of NGC 7252 are presented in Table 10.

The dynamical solution used to model NGC 7252 is taken from Borne & Richstone (1991, hereafter BR) in which two disks of equal mass merge from an initially close, elliptical, and fairly retrograde orbit (see Table 11). However, this solution

TABLE 10

NGC 7252 PROPERTIES

Property	Observed	Modeled	Notes
R.A. (2000.0)	$22^h17^m58^s$	...	1
Decl. (2000.0)	−24°55′48″	...	1
Heliocentric redshift	4760 km s^{-1}	...	1
Distance	48 Mpc	...	2
M_B	−20.8	...	3
Mass	$1.5 \times 10^{11}\ M_\odot$	$3.6 \times 10^{11}\ M_\odot$	4
Tail length	∼60 kpc	35 kpc	5
ΔV_{tails}	160 km s^{-1}	185 km s^{-1}	5
M_{gas}	$5.5 \times 10^9\ M_\odot$	$9.5 \times 10^9\ M_\odot$	6
SFR (FIR)	$7.9\ M_\odot$ yr^{-1}	$16\ M_\odot$ yr^{-1}	7

NOTES.—(1) From RC3. (2) Distance $= cz/H_0$. (3) $M_B = m_B + 5 - 5 \log (d)$, where $m_B = 12.6$ (RC3). (4) Derived using $(M/L)_B = 5\ M_\odot/L_\odot$. (5) From Schweizer 1982. (6) From Dupraz et al. 1990; Wang, Schweizer, & Scoville 1992; Hibbard et al. 1993. (7) FIR flux from Cataloged Galaxies and Quasars Observed in the *IRAS* Survey 1985; conversion to SFR from Hunter et al. 1986.

TABLE 11

NGC 7252 ORBIT

Parameter	Model Units	Scaled Units
Mass ratio	1:1	...
Orbit	Elliptical	...
Eccentricity	0.92	...
Semi-major axis	0.71	8.3 kpc
Disk 1 orientation	(150°, 45°)	...
Disk 2 orientation	(120°, 90°)	...
Viewing angle	(−15°, 25°)	...
Viewing time	3.7	185 Myr

presents a problem with initial conditions. Since the orbit derived by BR is one with an extremely close apocentric separation,[4] even starting the galaxies at apocenter means the disks are already in contact. At such a close separation, the practice of starting with pristine, cold disks seems very suspect indeed. The multiple three body technique employed by BR allows for a "relaxation phase" (Borne 1984) in which the galaxies adapt to the close presence of the companion, but no such correction is available via *N*-body dynamics. As shown by Borne (1984), starting a close orbit with such unrelaxed disks can lead to artificially short merger times.

The BR solution is modified slightly to account for the more massive galaxies used here ($M_{gal} = 1.3$, as opposed to $M_{gal,BR} = 1.0$) by scaling the distances up by a factor of 1.3. By doing so, the models are also corrected somewhat for the fact that the BR galaxies are more centrally concentrated than those presented here ($R_{1/2} = 0.5$, whereas $R_{1/2,BR} = 0.2$); however, the heightened dynamical friction caused by the more extended mass distribution inherent to the current models will again probably result in a more rapid merger than shown by BR. Finally, by moving the galaxies 30% further apart, the tidal tails will be shorter and less massive than otherwise modeled. It is important to keep these effects in mind while examining the NGC 7252 model.

The NGC 7252 model is observed at ∼200 Myr from the point of closest parabolic separation, from a viewing position 15° below the orbital plane and 25° behind the pericentric line. Figure 22 shows the stellar mass and star formation maps of the NGC 7252 model, while Figure 23 shows the model velocity field. The relative velocities of the tidal tails are reproduced, and the distribution of stellar mass shows an elliptical-like $r^{1/4}$ law. The velocity field in the main body, however, is much more smooth and regular than the observed velocity field (Schweizer 1982), most likely due to the coarse particle distribution and high velocity dispersion inherent to these models.

The model is viewed at a very early time, earlier than the $500\ h^{-1}$ Myr age implied by the observed tail kinematics (Schweizer 1982) and much earlier than shown by the dynamical model of BR. This discrepancy was anticipated due to the problem of initial conditions and the differing mass distributions between the current models and those of BR. The degree to which each process contributes to the discrepant merger times is difficult to evaluate; however, an examination of the merger times given by Borne (1984) show that the "relaxation" effect is less important for parabolic orbits than for circular

[4] Note that these orbital parameters do not imply that the disks have always been on such an orbit, only that the orbit has decayed to a point that is described by these parameters at the moment the interaction model is started.

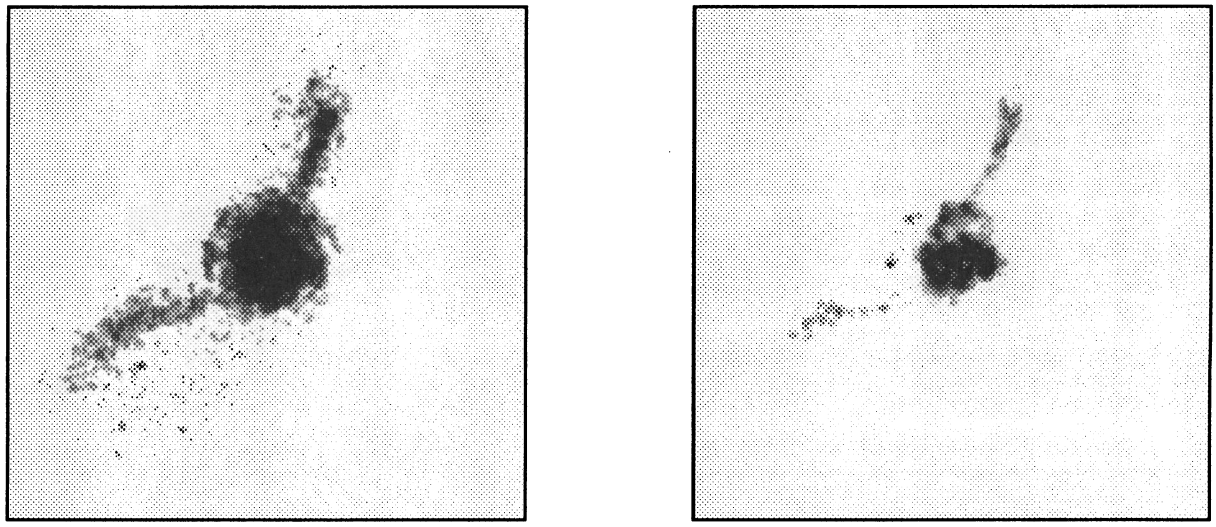

FIG. 22.—NGC 7252 model. (*a*) Stellar mass. (*b*) SFR map. To best show faint detail, both images are scaled logarithmically. North is up; east is to the left.

orbits. Since the ellipticity of the NGC 7252 model orbit is 0.92, nearly parabolic, it may be that the differing mass distribution contributes more to the increased braking than do the uncertain initial conditions. However, a third process also contributes to the decreased merging time—that of gasdynamical braking. As discussed in MRB, the dissipation of kinetic energy by the colliding ISMs can speed the merging process significantly. An analysis of the total energy of NGC 7252 system model shows that gasdynamical braking is responsible for shortening the merging timescale by $\sim 20\%$. Therefore, if the progenitor galaxies to NGC 7252 were embedded in diffuse halos and were sufficiently gas rich such that gasdynamical braking played a significant role, then the age of the NGC 7252 merger would be younger than the 800–1000 Myr age shown by the dynamical model of BR. The fact that the tail kinematics suggest a younger age of 500 Myr implies that these processes may have been important in the dynamical evolution of NGC 7252.

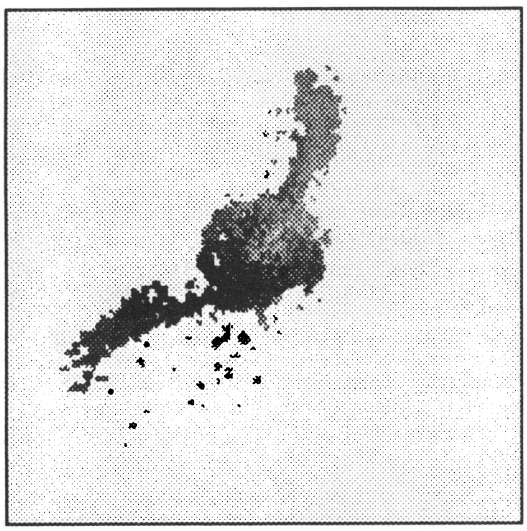

FIG. 23.—NGC 7252 model velocity field. Dark shading is redshifted; light shading is blueshifted.

The star-forming properties of the NGC 7252 model are dominated by the massive concentration of gas at the center of the merged system. The interaction has resulted in nearly 50% of the entire gas in the system being channeled into the central regions. This gas flow has triggered a very strong central starburst which at the present time is dying out due to an exhaustion of gas (Fig. 24). In fact, after a peak star formation rate of nearly 25 times the preinteraction rate, gas depletion has reduced the starburst intensity in NGC 7252 significantly, such that the current star formation rate in the NGC 7252 model is only one-third of the peak star formation rate. The spatial distribution of the modeled star formation is consistent with the observations of NGC 7252, which reveal a disk of ionized gas in the inner 2 kpc of the remnant (Schweizer 1982). Furthermore, the modeled gas depletion time for NGC 7252 is similar to the value of ~ 500 Myr derived from H I, H_2, and FIR observations as well. Finally, NGC 7252 also shows strong Balmer and Ca K absorption lines (Schweizer 1982), indicative of a strong population of luminous A stars, presumably formed in the strong merger-induced starburst.

Since NGC 7252 is the strongest interaction modeled of the five specific systems described here, and the most violent of the three merging systems modeled, it is interesting to ask if NGC 7252 ever went through an ultraluminous phase. Scaling the current FIR luminosity of NGC 7252 up by a factor of 3 would yield a luminosity of $L_{\rm FIR} \approx 4.5 \times 10^{10}\ L_\odot$, more than an order of magnitude fainter than the value of $\sim 10^{12}\ L_\odot$ displayed by the ultraluminous systems. The fact that such a strong interaction as NGC 7252 fails to produce an ultraluminous system reflects the severe difficulties in triggering such active systems. While the detailed accuracy of the NGC 7252 model is in question because of the uncertain merging timescale, it should be pointed out that a longer merging timescale would probably result in a less intense starburst (recall the relatively mild starbursts triggered by the merging of both the NGC 4038/39 system and the NGC 4676 system) as the gas will be slowly depleted before a major nuclear concentrations can develop.

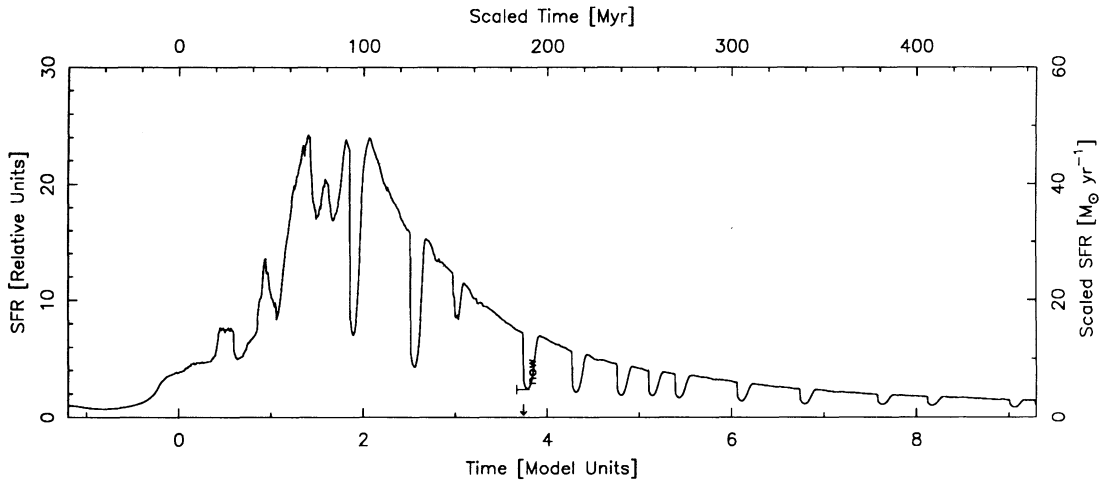

FIG. 24.—NGC 7252 model SFR evolution. Present time is denoted as T_{now}.

Therefore, the NGC 7252 model may overestimate, rather than underestimate, the induced starburst intensity.

The relationship between starburst strength and merger timescale leads to the following question: given the very high central star formation rates implied by the FIR emission from the ultraluminous IR galaxies, what constraints can be placed on the growth timescale for the central gas concentrations in these objects? A simple constraint would be that this growth timescale should be shorter than the gas depletion time of the starburst, or else star formation would deplete the ISM before the gas settles into the central regions. Extrapolating the Schmidt law employed in these models up to the gas densities displayed by systems such as Arp 220 or Arp 299 ($\rho_{gas} \sim 10^3$–$10^4\ M_\odot\ pc^{-3}$; Solomon, Downes, & Radford 1992) yields gas depletion times < 1 Myr. Since the observed gas depletion times (inferred from the FIR luminosity) are ~ 20 Myr, this discrepancy suggests that these starbursts are not well described by a simple extrapolation of a global Schmidt law up to such high densities—star formation takes place less efficiently than such a law implies. Furthermore, the short depletion times observed implies either that the gas must coalesce in a period much shorter than the merging timescale, or that star formation must be inhibited in some way during the coalescence period.

5. SUMMARY

This paper has presented models of five observed interacting systems in order both to examine specific instances of interaction-induced star formation and to test the detailed modeling process itself. Specific observations were done to facilitate a detailed comparison between observed and modeled kinematic and spatial distributions of star-forming gas. The systems were chosen to include a range of interaction types, from the passage of a small companion to a merger between two equal mass disks. Each system was modeled using the observed morphology and velocity field as a constraint to solve for the orbital parameters; once modeled, the predicted star-forming properties of each system were compared to the observed quantities.

In most cases, the models proved to reproduce the observed star-forming properties reasonably well in terms of spatial distribution and relative intensity of star formation. Absolute levels were less well modeled, not surprising considering the level of uncertainty in the observed masses, sizes, and gas mass fractions. Several modeled systems suggest that the models underestimate the importance of collisionally induced star formation. This limitation is probably due to the high velocity dispersion of the models, which tends to wash out small-scale structure, and perhaps an ISM which is too collisionless. Models with a larger number of particles would help reduce the large velocity dispersion, while a shortened mean free path for the clouds, or a more rigorous hydrodynamic approach to the ISM dynamics, would make the ISM more viscous and place more emphasis on the collisional aspect of the encounter.

The problem of not knowing the preencounter distribution of gas in each observed system presented a significant problem for the modeling process. Galaxies with a more extended distribution of gas tend to disperse more of their ISM into the surrounding medium than would galaxies with centrally peaked gas distributions. Since the strong starbursts are directly linked to channeling of large quantities of gas into the central regions, a more extended distribution of ISM gas could result in a lower starburst intensity. In the case of NGC 4038/39, the models suggest that a significant portion of the ISM was initially at large radii before the encounter, and differences between the observed and modeled properties of NGC 4676 and NGC 6872 could also be due to differing ISM distributions. Differing gas mass fractions also present a difficulty in the modeling process. The very low gas content of NGC 6872, for example, could explain the reason that elevated star formation rates did not accompany the formation of the stellar bar. Given the widely varying gas distributions displayed by individual galaxies, from exponential distributions of molecular gas to flat distributions of neutral gas, from H I holes to molecular rings, the problem of the uncertain preinteraction conditions of the ISM may represent a fundamental block to modeling specific interacting systems.

The observed properties of the interacting systems presented here also indicate that two differing triggers may be responsible for increased star formation rates. The nuclear starbursts displayed by NGC 4038/39, NGC 4676, and NGC 7252 result from large quantities of gas being funneled into the central regions of the galaxy. Observations of molecular gas in these systems show that the central gas densities can range from 10 to 10,000 $M_\odot\ pc^{-3}$. In such an environment, gravitational collapse is imminent, and so the high star formation

rates observed in these objects are simply a result of the very high gas densities caused by the interaction. However, several of the systems show evidence for collisionally triggered star formation. The fact that star formation is observed even in regions of high velocity dispersion in NGC 6872 and IC 1908 argues for star formation triggered by ISM collisions. Star formation in NGC 6872 is also closely linked to the tidal arms; the high velocity dispersion and velocity gradients associated with these features again suggests collisionally induced star formation is occurring.

Finally, of the five systems modeled, three of which either have merged or will merge, none ever experienced an ultraluminous phase of the type displayed by the ultraluminous infrared galaxies. This result once again demonstrates the rarity and difficulty in making such systems. In order for interaction-induced starbursts to trigger ultraluminous activity, at least three conditions must be met: the galaxies must merge, they must do so quickly, and they must have significantly high gas masses. If the galaxies merge slowly, on wide orbits, as was the case with NGC 4038/39 and NGC 4676, the gas is strongly depleted via star formation before the galaxies merge, limiting the intensity of the burst. Even if the galaxies merge quickly, as is the case with NGC 7252, without a significant amount of gas to fuel the starburst, the galaxies cannot produce enough star formation to boost the infrared luminosity to ultraluminous levels. Note that these conditions are not unrelated; a penetrating encounter between two gas-rich systems will experience strong gasdynamical braking (as shown in MRB) and ensure that the systems merge quickly. However, while such a scenario is consistent with the observed properties of the ultraluminous galaxies, these close, gas-rich encounters must be very rare, at least at the present time.

We thank the Kitt Peak National Observatory for the use of their Hα filter set used to image NGC 4676. In Chile, Bob Schommer was a tremendous help during the Fabry-Perot observing run at CTIO, and CTIO is thanked also for their financial contribution towards that run. On the computational side, we gratefully acknowledge Lars Hernquist for providing the original version of TREECODE from which these models were developed. J. C. M. thanks the Horace Rackham School for Graduate Studies at the University of Michigan for financial support. This research has made use of the NASA/IPAC Extragalactic Database (NED), which is operated by the Jet Propulsion Laboratory, Caltech, under contract with the National Aeronautics and Space Administration.

REFERENCES

Aaronson, M., et al. 1982, ApJS, 50, 241
Barnes, J. E. 1988, ApJ, 331, 699
Borne, K. D. 1984, ApJ, 287, 503
Borne, K. D., & Richstone, D. O. 1991, ApJ, 369, 111 (BR)
Bothun, G. D., Lonsdale, C. J., & Rice, W. 1989, ApJ, 341, 129
Bushouse, H. A. 1987, ApJ, 320, 49
Catalogued Galaxies and Quasars Observed in the *IRAS* Survey. 1985, prepared by C. J. Lonsdale, G. Helou, J. C. Good, & W. Rice (Washington: NASA)
de Vaucouleurs, G., de Vaucouleurs, A., Corwin, H. G., Buta, R. J., Paturel, G., & Foqué, P. 1991, Third Reference Catalogue of Bright Galaxies (New York: Springer-Verlag) (RC3)
Dupraz, C., Casoli, F., Combes, F., & Kazès, I. 1990, A&A, 228, L5
Gallagher, J. S., Hunter, D. A., & Tutukov, A. V. 1984, ApJ, 284, 544
Green, M. R., Godwin, J. G., & Peach, J. V. 1988, MNRAS, 234, 1051
Heckman, T. M. 1990, in IAU Colloq. 124, Paired and Interacting Galaxies, ed. J. W. Sulentic, W. C. Keel, & C. M. Telesco (Washington, DC: NASA), 359
Helou, G., Khan, I. R., Malek, L., & Boehmer, L. 1988, ApJS, 68, 151
Hernquist, L. 1987, ApJS, 64, 715
Hibbard, J. E., Guhathakurta, P., van Gorkom, J. H., & Schweizer, F. 1993, AJ, submitted
Hummel, E. 1981, A&A, 96, 111
Hunter, D. A., Gillett, F. C., Gallagher, J. S., Rice, W. L., & Low, F. J. 1986, ApJ, 303, 171
Joseph, R. D., Meikle, W. P. S., Robertson, N. A., & Wright, G. S. 1984, MNRAS, 209, 111
Kennicutt, R. C. 1989, ApJ, 344, 685
Kennicutt, R. C., Keel, W. C., van der Hulst, J. M., Hummel, E., & Roettiger, K. A. 1987, AJ, 93, 1011
Larson, R. B., & Tinsley, B. M. 1978, ApJ, 219, 46
Lonsdale, C. J., Persson, S. E., & Matthews, K. 1984, ApJ, 287, 95
Luppino, G. A. 1989, PASP, 101, 931
Massey, P., Strobel, K., Barnes, J. V., & Anderson, E. 1988, ApJ, 328, 315
Mazzarella, J. M., Bothun, G. D., & Boroson, T. A. 1991, AJ, 101, 2034
Mihos, J. C., Richstone, D. O., & Bothun, G. D. 1991, ApJ, 377, 72
———. 1992, ApJ, 400, 153 (MRB)
Noguchi, M. 1991, MNRAS, 251, 360
Noguchi, M., & Ishibashi, S. 1986, MNRAS, 219, 305
Olson, K. M., & Kwan, J. 1990a, ApJ, 349, 480
———. 1990b, ApJ, 361, 426
Phillips, A. C. 1993, Ph.D. thesis, Univ. of Washington
Reif, K., Mebold, U., Goss, W. M., van Woerden, H., & Siegman, B. 1982, A&AS, 50, 451
Schommer, R. A., Caldwell, N., Wilson, A. S., Baldwin, J. A., Phillips, M. M., Williams, T. B., & Turtle, A. J. 1988, ApJ, 324, 154
Schweizer, F. 1982, ApJ, 252, 455
Scoville, N. Z., Sanders, D. B., & Clemens, D. P. 1986, ApJ, 310, L77
Solomon, P. M., Downes, D., & Radford, S. J. E. 1992, ApJ, 387, L55
Stanford, S. A., Sargent, A. I., Sanders, D. B., & Scoville, N. Z. 1990, ApJ, 349, 492
Toomre, A. 1964, ApJ, 139, 1217
Toomre, A., & Toomre, J. 1972, ApJ, 178, 623 (TT)
Tubbs, A. D. 1982, ApJ, 255, 458
van der Hulst, J. M. 1979, A&A, 71, 131
Wang, Z., Schweizer, F., & Scoville, N. Z. 1992, ApJ, 396, 510
Young, J. S., & Scoville, N. Z. 1991, ARA&A, 29, 581